

Developed and Quasi-Developed Macro-Scale Heat Transfer in Micro- and Mini-Channels with Arrays of Offset Strip Fins Subject to a Uniform Heat Flux

A. Vangheffelen^{a,b,c,*}, G. Buckinx^{a,b,c}, C. De Servi^{b,c}, M. R. Vetrano^{a,c}, M. Baelmans^{a,c}

^a*Department of Mechanical Engineering, KU Leuven, Celestijnenlaan 300A, 3001 Leuven, Belgium*

^b*VITO, Boeretang 200, 2400 Mol, Belgium*

^c*EnergyVille, Thor Park, 3600 Genk, Belgium*

Abstract

In the present work, we examine to what degree the heat transfer can be described as developed on a macro-scale level in typical micro- and mini-channels with offset strip fin arrays subject to a uniform heat flux, considering flow entrance and side-wall effects. Full-scale numerical heat transfer simulations are conducted to determine the extent of the developed macro-scale heat transfer region within the arrays. We find that the onset point of developed heat transfer increases linearly with the Péclet number and channel width. However, the thermal development lengths remain limited relative to the overall channel length. Therefore, the local macro-scale heat transfer coefficient can be modeled by developed Nusselt number correlations with discrepancies below 25% in both the developed and developing heat transfer regions. We observe that quasi-developed heat transfer prevails over nearly the entire entrance region of the channel and significantly contributes to the main heat transfer characteristics, particularly the eigenvalues and amplitudes of the dominant temperature modes. Additionally, we analyze the impact of channel side walls on the temperature field's periodicity and the macro-scale temperature profile, which we characterize through an effective heat transfer coefficient. Our comprehensive numerical data covers various fin height-to-length ratios up to 1, fin pitch-to-length ratios up to 0.5, and channel aspect ratios ranging from 1/5 to 1/17, encompassing Reynolds numbers from 28 to 1224. Two sets of Prandtl number

*Corresponding author

Email address: arthur.vangheffelen@kuleuven.be. (A. Vangheffelen)

and thermal conductivity ratio are investigated, corresponding to the combinations of copper/air, and copper/water.

Keywords: Micro-and Mini-Channels, Offset Strip Fin Array, Macro-Scale Modeling, Quasi-Developed Heat Transfer, Closure

Nomenclature

Latin symbols

c	specific heat capacity, J/(kg K)
\mathbf{B}_{fm}	tensor that maps ∇T onto $\nabla \langle T \rangle_m^f$, -
\mathbf{B}_{sm}	tensor that maps ∇T onto $\nabla \langle T \rangle_m^s$, -
D	thermal dispersion source, m/(s K)
e	unit vector, -
h	fin height, m
h_{unit}	developed heat transfer coefficient, W/(m ³ K)
h_b	macro-scale heat transfer coefficient for bottom plate interface, W/(m ³ K)
h_{fs}	macro-scale heat transfer coefficient for fluid-solid interface, W/(m ³ K)
I	identity tensor, -
k	thermal conductivity, W/(m K)
\mathbf{K}_d	effective thermal dispersion tensor, m ² /s
\mathbf{K}_{fs}	effective interfacial heat transfer tensor, W/(m ² K)
\mathbf{K}_t	effective thermal tortuosity tensor, -
l	fin length, m
\mathbf{l}	lattice vector of unit cell, m
l_j	lattice size of unit cell, m
L_j	size of channel domain along e_j , m
m	normalized weighting function, -
\mathbf{n}	unit normal vector, -
N_j	number of unit cells along e_j , -
Nu	Nusselt number, -
Pe	Péclet number, -
Pr	Prandtl number, -
q	heat flux, W/m ²
Re	Reynolds number, -
s	fin pitch, m
s_0	length of inlet region in front of fin array, m
s_N	length of outlet region after fin array, m

t	fin thickness, m
T	temperature field, K
∇T	developed temperature gradient, K/m
u	velocity field, m/s
U_{dev}	developed macro-scale velocity, m/s
y	coordinate relative to center of filter window, m

Greek symbols

γ	phase indicator function, -
Γ	interface
δ	Dirac indicator function, -
ε	porosity, -
ε_0	perturbation size, -
Θ	temperature mode amplitude, K
κ	slope of macro-scale temperature difference profile, 1/m
λ	mode eigenvalue, -
μ	dynamic viscosity, Pa s
ξ	non-dimensional macro-scale profile, -
ρ	density, kg/m ³
ψ	vector field that maps ∇T onto T^* , m
Ψ	vector field that maps ∇T onto Θ , m
Ψ_0	closure variable amplitude, m
Ω	domain

Subscripts

<i>b</i>	related to the channel bottom plate / bulk average
dev	developed contribution
<i>e</i>	extension
<i>f</i>	restricted to the fluid
<i>fs</i>	related to the fluid-solid interface
in	related to the channel inlet
<i>m</i>	filtered by normalized weighting function <i>m</i>
out	related to the channel outlet
periodic	related to the periodically developed regime
predev	developing contribution
quasi-dev	related to the quasi-developed regime
quasi-periodic	related to the quasi-periodically developed regime
ref	used as reference
<i>s</i>	restricted to the solid
sides	related to the channel side walls
<i>t</i>	related to the channel top plate
T	related to the temperature
unit	unit cell
uniform	related to the uniform macro-scale regime

Superscripts

*	spatially periodic contribution
+	dimensionless
<i>f</i>	restricted to the fluid
<i>s</i>	restricted to the solid

1. Introduction

As energy systems, industrial processes, electronics and data centers demand ever increasing heat power densities, researchers have focused on developing more compact heat transfer devices. Over the past two decades, micro- and mini-channels with arrays of periodic fins have been shown to be very suitable for constructing highly-compact energy-efficient heat transfer devices [1, 2, 3, 4]. Particularly, micro- and mini-channels with periodic arrays of offset strip fins are frequently proposed as a solution, given that this fin type allows for high heat transfer coefficients and relatively low pressure drops. For that reason, they have been employed for the cooling of microelectronics [5, 6, 7], the recovery of waste heat in compact gas turbines [8, 9], the refrigeration and liquefaction in cryogenic systems [10, 11], and the heating of air flows in solar collectors [12, 13].

Our previous studies [14, 15] highlighted that the flow regime in micro- and mini-channels with arrays of offset strip fins is mainly laminar and steady [5, 6, 7, 8, 9, 10, 11, 12, 13, 16]. The corresponding heat transfer regime in these channels is characterized by the flow's Prandtl number, which is usually 0.7 or 7 since air and water are the most common working fluids [5, 6, 7, 8, 9, 12, 13, 16]. Nevertheless, the Prandtl number of cryogenic fluids like helium, hydrogen, and nitrogen, both in the gaseous and liquid state, is of the same order of magnitude as that of air [10, 11]. Furthermore, the heat transfer regime in micro- and mini-channel applications is commonly investigated under the assumption of a steady and uniform heat flux at the channel wall. This boundary condition is considered to represent well the heat transfer process in microelectronics cooling systems, balanced counter-flow heat recuperators, as well as solar air heaters, and heat exchangers in cryogenic systems [11, 12, 13, 17, 18, 19, 20, 21, 22].

To model the flow and heat transfer in micro- and mini-channels with large arrays of periodic solid structures, an analysis based on a single unit cell of the array is often preferred [23, 24]. After all, compared to a Direct Numerical Simulation (DNS) of the detailed heat transfer within the entire channel, a unit-cell approach significantly reduces the required computational resources [25]. In the scientific literature, two main theoretical frameworks can be distinguished that enable us to characterize the heat

transfer regime through a unit-cell simulation.

The first framework relies on the assumption that the heat transfer regime is periodically developed. That way, the temperature distribution in the channel can be obtained on a single unit cell by solving the periodic flow and heat transfer equations formulated by Patankar et al. [26]. These equations not only govern the periodic part of the temperature field, which is similar within every unit cell, but also the overall temperature gradient over each unit cell. This information allows us to obtain the total heat transferred between the fluid and the fins for any given flow rate.

The second framework treats the array of solid structures as a porous medium, allowing for the use of the volume-averaging technique (VAT) [27, 28] to determine the volume-averaged or *macro-scale* temperature field in the channel. In this approach, the macro-scale heat transfer rate at the fluid-solid interface is modelled as proportional to the difference in macro-scale temperatures of the fluid and solid, through the introduction of an interfacial heat transfer coefficient. This interfacial heat transfer coefficient is the solution to a closure problem that governs the local deviations from the macro-scale temperature field within the unit cell [27, 28]. In practice, however, this closure problem is rarely solved, as it long has been assumed equivalent to the periodic heat transfer equations formulated by Patankar et al. [26, 29, 30].

Yet, both frameworks can only be considered theoretically equivalent when specific weighting functions are selected to define the macro-scale temperature of the fluid and solid. In most cases, the equivalence of both frameworks requires the use of a double volume-averaging operation, as Buckinx and Baelmans ([31, 32, 33, 34]) demonstrated by extending the weighted volume-averaging technique proposed by Quintard and Whitaker [35, 36, 37, 38, 28, 39]. The double volume-averaging operation not only leads to a physically meaningful macro-scale description of the developed flow and heat transfer regimes, but it also gives rise to mathematically exact and spatially constant heat transfer coefficients obtainable from a unit-cell simulation.

In our previous works [14, 15, 40], we have studied the periodically developed flow and heat transfer regime in micro- and mini-channels with offset strip fin arrays subject to a uniform heat flux. Specifically, we have determined the macro-scale pressure gradient and macro-scale heat transfer coefficient for the periodically developed regime,

which we correlated in the form of a dimensionless friction factor and Nusselt number as a function of the Reynolds number, the geometrical parameters and the material properties. Moreover, using DNS, we have investigated to what extent the actual flow in the entire channel can be described as developed from a macro-scale perspective [40]. Notably, we have found that the flow becomes quasi-periodically developed close to the channel inlet and quickly decays to a fully periodic regime for a wide range of Reynolds numbers and geometrical parameters. As a result, the macro-scale flow is essentially developed over the entire channel, implying that our friction factor correlation [14] accurately predicts the overall pressure drop over the channel. These observations align with the work of Feppon [41], which mathematically proves the existence of quasi-periodically developed solutions for Stokes flow in finite periodic channels. It also presents an alternative macro-scale flow description based on formal two-scale asymptotic expansions.

Nevertheless, at present, it remains unclear how accurately our Nusselt number correlation [15] predicts the macro-scale heat transfer rate over the entire channel, or the overall temperature difference between the channel inlet and outlet. Ultimately, we still do not know at which distance from the channel inlet the heat transfer can be regarded as periodically developed in micro- and mini-channels with arrays of offset strip fins.

In the literature, very few studies treat the development of the heat transfer regime in channel flows. Most of the available studies consider the development of the temperature field in two-dimensional channels without solid structures. As they start from the ansatz that the flow is fully developed, i.e., Poiseuille flow, their main target is to solve the so-called Graetz-Nusselt problem for the channel's specific cross-sectional geometry [42, 43, 44]. Hereto, two solution methods are commonly applied, both yielding the thermal development length, as well as the incremental heat transfer rate in the channel entrance region.

The first solution method, proposed by Graetz, consists of applying separation of variables to the developing temperature field, so that the separated problem becomes solvable via Sturm-Liouville theory [42]. This means that the solution for the temperature field is obtained as an infinite series of eigenvalues and eigenfunctions for the

Graetz-Nusselt problem.

A second solution method is the L ev eque approach, which supplements the Graetz method with a similarity transformation. The purpose of the similarity transformation is to circumvent the need for an increasingly large number of terms in the series solution for the temperature field to obtain a good accuracy near the channel inlet [45, 46].

Also, numerical methods have been employed to study the development of the heat transfer regime. Such methods usually rely on a finite-difference or finite-volume discretization to solve the thermal energy equation [47, 48, 49]. As a matter of fact, numerical methods have been the only means so far to determine the developing temperature field in a simultaneously developing flow. Especially when the flow is turbulent instead of laminar, or the considered channel geometry is three-dimensional instead of two-dimensional, numerical methods have found widespread application, though only for channels without solid structures [50, 51, 52, 53].

On the contrary, no numerical or analytical studies exist in the literature on the development of heat transfer in channels with arrays of fins or other solid structures. Further progress on the topic appears to be hampered by the tremendously high computational cost of DNS for resolving the flow and temperature fields in large arrays [25]. As a result, the general features of the developing flow and heat transfer in such channels are still barely understood, with the exception of the quasi-periodically developed flow regime [54]. The former regime is characterized by a single exponential velocity mode with a streamwise periodic amplitude and dominates over almost the entire entrance region in micro- and mini-channels with offset strip fins [40] and inline cylinders [55]. Although the existence of a similar quasi-periodically developed heat transfer regime has also been recently deduced [56], its significance within the entire region of developing heat transfer has yet to be investigated, as empirical data is still lacking.

Not only theoretical work, but also experimental work on the heat transfer development in channels with arrays of solid structures remains scarce. To the authors' knowledge, the study by Dong et al. [57] provides the only experimental investigation of the influence of thermal development on the thermo-hydraulic performance of offset strip fin arrays. Dong et al. present a correlation for the Colburn j -factor, which repre-

sents the overall heat transfer coefficient in the channel measured through temperature probes upstream and downstream of various air-side offset strip fin arrays. In this correlation, the influence of the developing flow and heat transfer regime has been taken into account via a scaling factor based on the ratio of the total channel length to the offset strip fin length. It should be noted, though, that the correlation mainly covers data for air flows in the transitional regime and applies only to conventional offset strip fin channels with relatively high channel heights. Moreover, as the heat transfer data was obtained using high flow rates of hot water on the control side, the correlation reflects a constant wall temperature condition rather than a constant heat flux boundary condition. Therefore, the analysis of Dong et al. is of limited significance for micro- and mini-channels with offset strip fin arrays, particularly when the heat flux at the wall is imposed.

From the preceding literature survey we conclude that, currently, the importance of the heat transfer development in micro- and mini-channels with offset strip fin arrays is still unexplored. Therefore, this work numerically assesses to what extent the heat transfer regime can be described as developed on a macro-scale level in common micro- and mini-channels with offset strip fins subject to a uniform heat flux. Specifically, we analyze the onset point of the developed heat transfer regime, as well as the onset point of quasi-developed heat transfer inside these channels. Hereto, we rely on DNS to resolve the entire temperature field in the simultaneously developing channel flow for Reynolds numbers ranging from 28 to 1224. Both air and water are considered as working fluids, each in combination with a highly thermally conductive solid material, such as copper. Further, we assess the accuracy of the Nusselt number correlations from our preceding work [15] in the region where the heat transfer regime is still developing, since they are strictly speaking only valid for predicting the heat transfer coefficient in the developed region. Concretely, we conduct a comparison with the actual macro-scale heat transfer coefficient along the channel, which we compute from the full temperature field through a discretized double volume-averaging operator. Finally, we investigate and quantify the influence of the channel's side walls on the developed macro-scale temperature field and the actual macro-scale heat transfer coefficient.

The present work is structured as follows. Section 2 focuses on DNS, where we present the geometry of the channels and offset strip fins, the computational domain, the energy equations for steady conjugate heat transfer in the channel, as well as the numerical procedure to solve them. In Section 3, the onset of the developed macro-scale heat transfer is determined, and the validity of our developed Nusselt number correlations is discussed. The onset point and features of the quasi-developed heat transfer regime are presented in Section 4. Lastly, Section 5 treats the influence of the channel side wall on the macro-scale heat transfer.

2. Channel geometry and (macro-scale) temperature equations

2.1. Geometry of the channel and fin array

Figure 1 illustrates the channel domain Ω used for the direct numerical simulation (DNS) of the three-dimensional temperature field inside. The channel contains an offset strip fin array comprising N_1 unit cells along the main flow direction and N_2 unit cells along the lateral direction. The channel's total length L_1 , total width L_2 and total height L_3 are given by $L_1 = (s_0 + N_1 l_1 + s_N)$, $L_2 = N_2 l_2$ and $L_3 = l_3$, since s_0 and s_N denote the distance between the fin array and channel inlet or outlet, respectively. We remark that the channel walls have zero thickness. Also, a single unit cell Ω_{unit} of the offset strip fin array is shown in Figure 1. The geometry of the unit cell is determined by the fin length l , the fin height h , the lateral fin pitch s , and the fin thickness t . The porosity of the fin array is thus given by $\varepsilon_f = hs / [(h+t)(s+t)]$. Each unit cell is spanned by three lattice vectors $\boldsymbol{l}_1 = l_1 \boldsymbol{e}_1 = 2l \boldsymbol{e}_1$, $\boldsymbol{l}_2 = l_2 \boldsymbol{e}_2 = 2(s+t) \boldsymbol{e}_2$ and $\boldsymbol{l}_3 = l_3 \boldsymbol{e}_3 = (h+t) \boldsymbol{e}_3$ with respect to the normalized Cartesian vector basis $\{\boldsymbol{e}_j\}_{j=1,2,3}$, as depicted in Figure 1.

In this work, the following array sizes have been selected for our DNS simulations: $N_1 = 20$, $N_2 \in \{5, 10, 13, 15, 17\}$. Furthermore, an inlet and outlet region without fins over a length $s_0 = l_1$ and $s_N = 2.5l_1$ have been added in front and behind the offset strip fin array. These parameter values are the same as those considered in our previous study on the macro-scale flow development in offset strip fin arrays [58]. They have been chosen such that our results are representative of typical geometries of micro- and

mini-channels with offset strip fins [5, 6, 7, 8, 9, 10, 11, 12, 13]. We have verified that the number of fin rows $N_1 = 20$ is large enough to accurately assess the development lengths for both the flow and temperature fields. Besides, we have checked that the number of lateral unit cells N_2 results in true lateral periodicity of the flow field at a distance l_2 from the channel's sidewalls.

It is worth noting that if we use the fin length l as the reference length, the non-dimensional geometrical parameters h/l , s/l , t/l , s_0 , s_N , N_1 , and N_2 completely specify of the channel geometry.

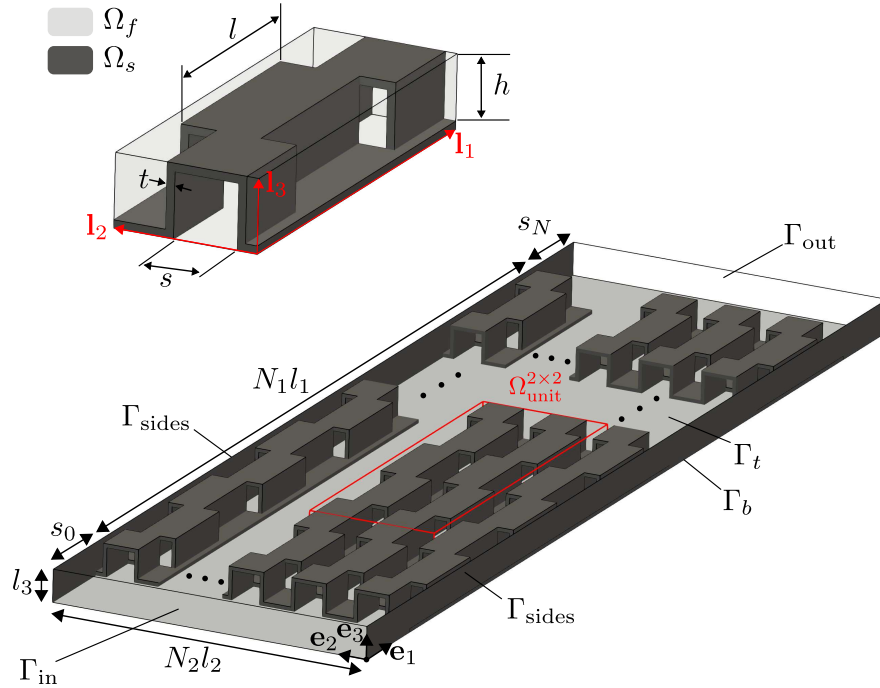


Figure 1: Offset strip fin channel and unit cell domain

2.2. Temperature equations for steady conjugate heat transfer in a channel

The temperature field T in the channel Ω , which equals T_f in the fluid (Ω_f) and T_s in the solid material (Ω_s), is obtained from the following energy conservation equations, as we neglect viscous dissipation and other heat sources:

$$\begin{aligned}\rho_f c_f \nabla \cdot (\mathbf{u} T_f) &= k_f \nabla^2 T_f & \text{in } \Omega_f, \\ 0 &= k_s \nabla^2 T_s & \text{in } \Omega_s,\end{aligned}\tag{1}$$

Here, the thermal conductivity k , density ρ , and specific heat capacity c of the fluid (f) and solid (s) are all assumed to be constant. The steady velocity field \mathbf{u} has been obtained by solving the Navier-Stokes equations for an incompressible Newtonian fluid determined, as described in [58].

We consider the following boundary conditions for the temperature field in the channel. At the channel inlet Γ_{in} , a uniform inlet temperature T_{in} is assumed. A uniform heat flux q_b is imposed at the bottom wall of the channel, which is further subdivided into a part that bounds the fluid domain and a part that bounds the solid domain: $\Gamma_b = \Gamma_{bf} \cup \Gamma_{bs}$. At the channel outlet Γ_{out} , the top boundary Γ_t and the side-wall boundaries Γ_{sides} , a no-heat-flux boundary condition, hence a zero Neumann boundary condition, is assumed. Finally, at the fluid-solid interface Γ_{fs} , we assume the continuity of the temperature field and the heat flux to adequately model the steady conjugate heat transfer between the fluid and solid. Mathematically, the former boundary conditions have the following form:

$$\begin{aligned}T_f(\mathbf{x}) &= T_{\text{in}} & \text{in } \Gamma_{\text{in}}, \\ -\mathbf{n} \cdot k_f \nabla T_f &= q_b & \text{in } \Gamma_{bf}, \\ -\mathbf{n} \cdot k_s \nabla T_s &= q_b & \text{in } \Gamma_{bs}, \\ -\mathbf{n} \cdot k_f \nabla T_f &= 0 & \text{in } \Gamma_{\text{out}} \cup \Gamma_t \cup \Gamma_{\text{sides}}, \\ -\mathbf{n} \cdot k_s \nabla T_s &= 0 & \text{in } \Gamma_t \cup \Gamma_{\text{sides}}, \\ T_f &= T_s & \text{in } \Gamma_{fs}, \\ -\mathbf{n}_{fs} \cdot k_f \nabla T_f &= -\mathbf{n}_{fs} \cdot k_s \nabla T_s & \text{in } \Gamma_{fs}.\end{aligned}\tag{2}$$

We remark that in the boundary conditions (2), the unit normal vector \mathbf{n} at the exterior boundary $\Gamma = \partial\Omega$ points outward of the channel domain Ω . As a result, the heat flux

q_b is negative when it is directed towards the channel Ω . On the other hand, the unit normal vector \mathbf{n}_{fs} at Γ_{fs} points from the fluid domain Ω_f towards the solid domain Ω_s .

The former temperature equations (1) and their boundary conditions (2) are solved for two Prandtl numbers: $Pr_f = 0.7$ and $Pr_f = 7$, which correspond to air and water as the fluid. Moreover, we have computed solutions for two thermal conductivity ratios: $k_s/k_f = 10^4$ and $k_s/k_f = 500$. These ratios have been selected to represent the combinations of copper/air, and copper/water, respectively [59]. The former thermal parameters are consistent with our previous study on the periodically developed heat transfer regime mini- and micro-channels with offset strip fins [15].

2.3. Macro-scale temperature equations for steady conjugate heat transfer in a channel

In agreement with the macro-scale descriptions from [31, 32, 33, 34, 35, 55, 58], we compute the macro-scale temperature fields by applying a double volume-averaging operator $\langle \cdot \rangle_m$ to the original temperature fields T_f and T_s . This operator corresponds to the convolution product $\langle \phi \rangle_m = m * \phi$ in \mathbb{R}^3 with the weighting function

$$m(\mathbf{y}) = \frac{1}{l_3} \text{rect}\left(\frac{y_3}{l_3}\right) \prod_{j=1}^2 \frac{l_j - 2|y_j|}{l_j} \text{rect}\left(\frac{y_j}{2l_j}\right). \quad (3)$$

Because this weighting function is based on the normalized rectangle function [60], its filter window is a double unit cell $\Omega_{\text{unit}}^{2 \times 2}(\mathbf{x})$ with the same height as the channel [55] (see Figure 1). Consequently, the resulting macro-scale variables are two-dimensional fields: they vary only with the coordinate position in the midplane of the channel on which they are evaluated.

In particular, we define the intrinsic macro-scale temperatures of the fluid and solid as $\langle T \rangle_m^f \triangleq \varepsilon_{fm}^{-1} \langle T \gamma_f \rangle_m$ and $\langle T \rangle_m^s \triangleq \varepsilon_{sm}^{-1} \langle T \gamma_s \rangle_m$, respectively. Here, we have introduced the fluid indicator γ_f and solid indicator γ_s , which are given by $\gamma_f(\mathbf{x}) = 1 \leftrightarrow \mathbf{x} \in \Omega_f$, $\gamma_f(\mathbf{x}) = 0 \leftrightarrow \mathbf{x} \in \mathbb{R}^3 \setminus \Omega_f$ and $\gamma_s(\mathbf{x}) = 1 \leftrightarrow \mathbf{x} \in \Omega_s$, $\gamma_s(\mathbf{x}) = 0 \leftrightarrow \mathbf{x} \in \mathbb{R}^3 \setminus \Omega_s$. Further, the weighted porosities are defined by $\varepsilon_{fm} \triangleq \langle \gamma_f \rangle_m$ and $\varepsilon_{sm} \triangleq \langle \gamma_s \rangle_m$.

The intrinsic macro-scale temperature fields of the fluid and solid are governed by

the following macro-scale energy conservation equations [28, 34]:

$$\begin{aligned}
\rho_f c_f \nabla \cdot (\boldsymbol{\varepsilon}_{fm} \langle \mathbf{u} \rangle_m^f \langle T \rangle_m^f) &= k_f \nabla^2 (\boldsymbol{\varepsilon}_{fm} \langle T \rangle_m^f) - \langle q_b \boldsymbol{\delta}_{bf} \rangle_m - \rho_f c_f \nabla \cdot \mathbf{D} \\
&+ k_f \nabla \cdot \langle \mathbf{n}_{fs} T_f \boldsymbol{\delta}_{fs} \rangle_m + k_f \nabla \cdot \langle \mathbf{n} T_f \boldsymbol{\delta}_{sides,f} \rangle_m \\
&+ k_f \langle \mathbf{n}_{fs} \cdot \nabla T_f \boldsymbol{\delta}_{fs} \rangle_m \\
\mathbf{0} &= k_s \nabla^2 (\boldsymbol{\varepsilon}_{sm} \langle T \rangle_m^s) - \langle q_b \boldsymbol{\delta}_{bs} \rangle_m \\
&- k_s \nabla \cdot \langle \mathbf{n}_{fs} T_s \boldsymbol{\delta}_{fs} \rangle_m + k_s \nabla \cdot \langle \mathbf{n} T_s \boldsymbol{\delta}_{sides,s} \rangle_m \\
&- k_s \langle \mathbf{n}_{fs} \cdot \nabla T_s \boldsymbol{\delta}_{fs} \rangle_m.
\end{aligned} \tag{4}$$

In these energy equations, five closure terms can be distinguished. First, we have the macro-scale thermal dispersion source, $\mathbf{D} \triangleq \langle \mathbf{u} T \rangle_m - \boldsymbol{\varepsilon}_{fm} \langle \mathbf{u} \rangle_m^f \langle T \rangle_m^f$. This closure term represents the advective heat transfer that occurs by the local fluid velocity variations on top of the intrinsic macro-scale velocity $\langle \mathbf{u} \rangle_m^f \triangleq \boldsymbol{\varepsilon}_{fm}^{-1} \langle \mathbf{u} \boldsymbol{\gamma}_f \rangle_m$. Secondly, we have the macro-scale thermal tortuosity, $\langle \mathbf{n}_{fs} T_f \boldsymbol{\delta}_{fs} \rangle_m = \langle \mathbf{n}_{fs} T_s \boldsymbol{\delta}_{fs} \rangle_m$, which is based on the Dirac surface indicator $\boldsymbol{\delta}_{fs}$ for Γ_{fs} . This closure term thus expresses a boundary integral of the temperature field over the curved (hence "tortuous") part of the fluid-solid interface contained within the filter window. Thirdly, we have the macro-scale interfacial heat transfer through conduction from the fluid to the solid along their interface Γ_{fs} inside the filter window:

$$\langle q_{fs} \boldsymbol{\delta}_{fs} \rangle_m = -k_f \langle \mathbf{n}_{fs} \cdot \nabla T_f \boldsymbol{\delta}_{fs} \rangle_m = -k_s \langle \mathbf{n}_{fs} \cdot \nabla T_s \boldsymbol{\delta}_{fs} \rangle_m. \tag{5}$$

Similarly, we recognize the macro-scale heat transfer imposed at the bottom of the channel, $\langle q_b \boldsymbol{\delta}_b \rangle_m$, which can be split into the contributions $\langle q_{bf} \boldsymbol{\delta}_{bf} \rangle_m$ and $\langle q_{bs} \boldsymbol{\delta}_{bs} \rangle_m$, from the surfaces Γ_{bf} and Γ_{bs} respectively. Finally, we have the two thermal tortuosity terms due to the channel's side walls, $k_f \nabla \cdot \langle \mathbf{n} T_f \boldsymbol{\delta}_{sides,f} \rangle_m$ and $k_s \nabla \cdot \langle \mathbf{n} T_s \boldsymbol{\delta}_{sides,s} \rangle_m$. They are based on the Dirac surface indicators $\boldsymbol{\delta}_{sides,f}$ and $\boldsymbol{\delta}_{sides,s}$ corresponding to the part of Γ_{sides} which bounds Ω_f and Ω_s , respectively.

It should be noted that the former macro-scale temperature equations are technically only valid when the overall temperature field T is interpreted as an extended distribution of the form $T = T_f$ in Ω_f , $T = T_s$ in Ω_s and $T = T_e$ in $\mathbb{R}^3 \setminus \Omega$. In this work, the extension T_e has been determined by extrapolation from the channel inlet, channel outlet, top boundary, and bottom boundary: $\forall s > 0 : T_e(\mathbf{x} + s\mathbf{n}) = T_f(\mathbf{x})$

when $\mathbf{x} \in (\Gamma_{\text{in}} \cup \Gamma_{\text{out}} \cup \Gamma_{\text{t}} \cup \Gamma_{\text{b}})$. Away from the channel side walls, we select $\forall s > 0 : T_e(\mathbf{x} + s\mathbf{n}) = 0$ when $\mathbf{x} \in \Gamma_{\text{sides}}$. In this manner, we avoid the necessity to include additional closure terms in (4), the so-called commutation errors, which arise due to discontinuous temperature jumps at the domain boundaries [34].

In line with the literature [32, 33], we represent the macro-scale heat transfer rate at the fluid-solid interface by means of an interfacial heat transfer coefficient:

$$h_{fs} \triangleq \varepsilon_{fm}^{-1} \frac{\langle q_{fs} \delta_{fs} \rangle_m}{\langle T \rangle_m^f - \langle T \rangle_m^s}. \quad (6)$$

The latter is related to the non-dimensional Nusselt number $Nu_{fs} \triangleq h_{fs} l^2 / k_f$. In this work, we also make use of the following macro-scale heat transfer coefficient to represent the macro-scale heat transfer rate at the channel's bottom wall:

$$h_b \triangleq \varepsilon_{fm}^{-1} \frac{\langle q_b \delta_b \rangle_m}{\langle T \rangle_m^f - \langle T \rangle_m^s}, \quad (7)$$

so we define $Nu_b \triangleq h_b l^2 / k_f$.

2.4. Numerical procedure

To solve the temperature equations (1)-(2), we used the software package FEniCSLab, which was developed by G. Buckinx within the finite-element computing platform FEniCS [61]. A structured mesh was used for the spatial discretization of the offset strip fin channel, identical to the one employed for the flow simulations in our previous work [58]. The reason is that the developing velocity fields were also obtained from that work. The temperature field has been discretized by continuous Galerkin tetrahedral elements of the second order. Each temperature simulation required a computational time of at most 30 minutes on 10 nodes with 36 processors each (Xeon Gold 6140 2.3GHz with 192GB of RAM). The algebraic linear system of discretized temperature equations was solved iteratively using the generalized minimal residual method (GMRES) method with a Jacobi preconditioner [62]. For all the cases considered in this work, a mesh-independence study has been performed, which indicated that the discretization error on the temperature profiles remains below 3%. Finally, the same explicit finite-element integral operator as in [58] has been used for the double volume-averaging operations. The former was implemented in FEniCSLab

by G. Buckinx [55]. For each temperature field, the calculation of the discrete double volume-averaging operation took about 6 hours on 10 nodes with 36 processors (Xeon Gold 6140 2.3GHz with 192GB of RAM).

Figure 2 illustrates the simulated temperature field in an offset strip fin channel for a Prandtl number $Pr_f = 7$ and a Reynolds number $Re_b \triangleq \rho_f u_b (2L_3) / \mu_f = \rho_f u_b 2(h + t) / \mu_f = 28$, based on the the bulk average velocity u_b as defined in [58]. The considered geometry is specified by $h/l = 0.12$, $s/l = 0.48$, $t/l = 0.02$, $s_0 = l_1$, $s_N = 2.5l_1$, $N_1 = 20$, and $N_2 = 10$. The temperature profiles are visualized through iso-lines of the non-dimensional temperature $T^+ \triangleq (T - T_{in})k_f / (q_b l)$ in the mid-plane of the channel, spanned by e_1 and e_2 . To ensure the clarity of the figure, only half of the region near the channel inlet is shown. It is clear that, after a short distance from the start of the fin array (at $x_1 \simeq 2l_1$), the temperature profiles around the offset strip fins in the array appear to become qualitatively similar, despite the presence of some irregularities, which are artefacts resulting from the employed visualization software [63]. This similarity in the temperature field indicates the occurrence of the periodically developed heat transfer regime.

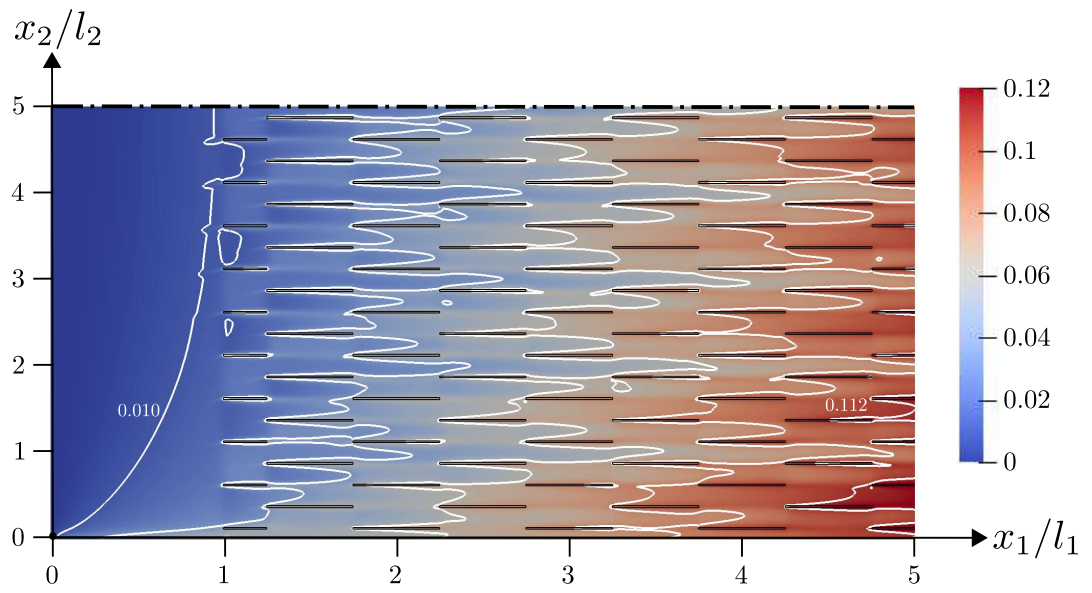


Figure 2: The non-dimensional temperature field $T^+ \triangleq (T - T_{in})k_f/(q_b l)$ in an offset strip fin channel for $Pr_f = 7$, $Re_b = 28$, $h/l = 0.12$, $s/l = 0.48$, $t/l = 0.02$, $s_0 = l_1$, $s_N = 2.5l_1$, $N_1 = 20$, and $N_2 = 10$. Its iso-lines are shown in half of the mid-plane spanned by e_1 and e_2 . The black rectangles indicate the outlines of the offset strip fins.

3. Onset of developed macro-scale heat transfer

We first examine the onset point of the periodically developed heat transfer regime by analyzing the computed temperature fields of the air and water flows for various Reynolds numbers and channel geometries. This onset point also marks the onset of the developed macro-scale heat transfer regime, as the latter occurs at most a distance l_1 further downstream along the main flow direction e_1 . The reason for this is that l_1 is the filter radius of the double volume-averaging operator (3), hence the length scale over which local temperature gradients are smoothed in our macro-scale description.

3.1. Onset of periodically developed heat transfer

As we consider a constant heat flux at the channel wall, the periodically developed heat transfer regime is characterized by a linearly varying temperature field, on which a streamwise periodic temperature part is superposed [26, 64]:

$$T \simeq T_{\text{dev}} \triangleq \nabla T \cdot \boldsymbol{x} + T^*. \quad (8)$$

Here, ∇T is the spatially constant overall temperature gradient, while the periodic temperature part satisfies $T^*(\boldsymbol{x} + \boldsymbol{l}_1) = T^*(\boldsymbol{x})$, just like the streamwise periodic velocity field $\boldsymbol{u} = \boldsymbol{u}^*$ in this region.

Accordingly, we define the onset point $x_{\text{periodic},T}$ of the periodically developed heat transfer regime as the streamwise coordinate x_1 after which the temperature field agrees with the periodically developed solution (8) within 10% of the overall temperature change over a single unit cell, so $|T - T_{\text{dev}}|/|\nabla T \cdot \boldsymbol{l}_1| \leq 0.1$ for $x_1 \geq x_{\text{periodic},T}$. The practical advantage of this definition lies in the fact the value of $x_{\text{periodic},T}$ remains independent of the total array length. Moreover, due to the employed criterion for defining $x_{\text{periodic},T}$, we can generally expect expression (8) to hold within at least 1% of the total temperature difference over the entire developed region. The explanation is that the developed region reasonably covers more than 10 unit cells in the streamwise direction, given the high number of fin rows in contemporary micro- and mini-channels [5, 6, 7, 8, 9, 10, 11, 12, 13]. Another interesting consequence of the chosen criterion is illustrated later in this section: For all the cases examined in this study, the local

macro-scale heat transfer coefficient and local Nusselt number along the centerline of the channel are observed to deviate at most 5% from their constant values in the developed region, when this region is identified as $x_1 \geq x_{\text{periodic,T}}$.

In Figure 3, the onset point $x_{\text{periodic,T}}$ has been quantified for an array with 10 offset strip fins along the lateral direction, having a small height ($h/l = 0.12$) and moderate spacing ($s/l = 0.48$). In particular, the dependence of the onset point $x_{\text{periodic,T}}$ on the bulk Reynolds number Re_b and the Prandtl number Pr_f is illustrated. The error bars in the figure indicate the numerical uncertainty associated with discretization errors. Clearly, a linear relationship can be observed between the onset point $x_{\text{periodic,T}}$ and the Reynolds number Re_b . This linear relationship is inherited from the onset point of the periodically developed flow regime [58]. Indeed, before the temperature field can become developed, first the flow field itself must become (close to) developed, so both onset points will tend to move more downstream at a similar rate as Re_b increases.

Figure 3 shows that the relation between the onset point $x_{\text{periodic,T}}$ and the Prandtl number Pr_f can be reduced to a linear dependence on the Péclet number $Pe \triangleq Re_b Pr_f$. This appears to be true for all geometries and flow conditions studied in this work. We found, for instance, that the data in Figure 3 is captured by the following linear correlations to within a maximum error of 5%: $(x_{\text{periodic,T}} - s_0)/l_1 \simeq 0.0214Pe - 0.899$ when $t/l = 0.02$, and $(x_{\text{periodic,T}} - s_0)/l_1 \simeq 0.0198Pe - 0.680$ when $t/l = 0.04$. It should be noted though that the former linear correlations are only valid for $Pe > 42$ and $Pe > 34$, respectively. For smaller values of the Péclet number, the onset point approximately coincides with the start of the fin array: $x_{\text{periodic,T}} \simeq s_0$, as it can be seen in Figure 3.

The linear relationship between the onset point and Péclet number $x_{\text{periodic,T}}/l_1 \simeq APe + B$, with A and B some constants, reflects that the distance over which the temperature field develops, is essentially determined by the rate at which thermal energy diffuses perpendicularly to the main flow direction, once the flow field has become developed. After all, the rate of thermal diffusion is given by $1/Pe$ when compared to the rate of thermal advection in the main flow direction.

The fact that $x_{\text{periodic,T}}$ increases with Pe also indicates that the Prandtl number Pr_f is a measure for the spatial distance over which the onset of developed heat transfer

lags with respect to the onset of developed flow. This should be no surprise, since development essentially occurs through the diffusion of momentum and thermal energy in the directions perpendicular to the bulk flow, while the Prandtl number can be interpreted as the relative strength of thermal diffusion compared to momentum diffusion. For that reason, the onset point $x_{\text{periodic,T}}$ is located upstream of the onset point x_{periodic} of the periodically developed flow regime when $Pr_f = 0.7$ [58]. On the contrary, when $Pr_f = 7$, $x_{\text{periodic,T}}$ and x_{periodic} have a comparable magnitude, although their ratio is heavily dependent on the precise criterion used for defining $x_{\text{periodic,T}}$ and x_{periodic} .

The observation that the onset point of the periodically developed heat transfer regime depends only on the Péclet number implies that this onset point is not influenced by the fluid's viscosity. This is a direct similarity between micro- or mini-channel with offset strip fins and other channels without solid structures. In fact, a linear scaling of the onset point with the Péclet number has been shown to occur in channels with a fixed hydraulic cross-section, not only when the heat transfer and flow regime are developing simultaneously [65], but also when the flow regime is already fully developed [66, 67, 68].

Despite this similarity, it should be noted that the thermal development lengths ($x_{\text{periodic,T}} - s_0$) from this work cannot be obtained by simply re-scaling the flow development lengths from our previous work [58] with the Prandtl number: $x_{\text{periodic,T}} \neq x_{\text{periodic}} Pr_f$. This is a significant difference from what has been observed for flows in channels without solid structures [65], as well as external boundary-layer flows [69]. Yet, we hypothesize that this difference can be attributed to the fact that in such types of flow, the streamwise diffusion of momentum and thermal energy is less important than in channels with fin arrays. In boundary-layer flows and channel flows of which the cross-sectional area does not change, streamwise diffusion of momentum and thermal energy is almost entirely overshadowed by streamwise advection of momentum and thermal energy. Consequently, the former's effect on the development lengths can be ignored because the characteristic length scale for streamwise advection is also quite large, typically comparable to the channel length. On the contrary, in channels containing a fin array, the characteristic length scale for streamwise advection is much smaller, often comparable to the spatial period l_1 of the array. The reason is that the steady flow

patterns in a fin array, like wakes, recirculation zones, and vortices induced by the periodic variations in cross-sectional flow area are confined by the space between the periodic solid structures.

In Figure 3, we have also illustrated the influence of the fin thickness-to-length ratio t/l on the onset point of the periodically developed heat transfer regime. It can be seen that the thickness ratio t/l has only a minimal influence on the onset point $x_{\text{periodic,T}}$. This is because the ratio t/l has no significant impact on the onset point of periodically developed flow either [58].

Conversely, the aspect ratio of the channel $L_3/L_2 = l_3/(N_2l_2)$ does have a significant impact on the onset point, as Figure 4 shows. This figure shows that the onset point will move several unit cells more downstream when the aspect ratio of the channel decreases, hence when the number of unit cells in the lateral direction N_2 increases. The relationship between $x_{\text{periodic,T}}$ and N_2 is almost perfectly linear, as the straight lines in Figure 4 capture the data points with a maximum relative error of 5%. This finding aligns with the observed linear relation between the flow development length and channel width in the same channels [58]. From a physical point of view, the linear scaling can be explained by noting again that thermal development occurs mostly due to lateral diffusion of thermal energy until all upstream perturbations from the developed temperature profile are leveled off. As the width of the channel corresponds to the distance over which these perturbations need to be transported via lateral diffusion, a higher channel width will result in a proportionally longer diffusion time and, consequently, a proportionally longer development length.

Also, in rectangular channels without solid structures, the thermal development length increases for decreasing aspect ratios, although not necessarily in an inversely linear fashion [66, 67, 68]. However, in those studies, the aspect ratio values are much larger than those in this work. Therefore, a direct comparison cannot be made.

Next to the aspect ratio, also the fin height-to-length ratio h/l has a significant influence on the onset point $x_{\text{periodic,T}}$, as illustrated in Figure 5. In this figure, we have kept the bulk velocity u_b and fin length l constant to highlight the isolated effect of changing the fin height-to-length ratio h/l . Hereto, we have specifically selected $Re_b l / (2L_3) = \rho_f u_b l / \mu_f = 600$, which implies that the bulk Reynolds number

Re_b varies within the range of (168, 1224) for $h/l \in (0.12, 1)$.

We can distinguish two trends in Figure 5. First, we observe that the onset point $x_{\text{periodic,T}}$ moves downstream as the fin height-to-length ratio h/l increases. This comes from the fact that the fin height h , just like the channel width L_2 , is a distance over which upstream perturbations from the developed temperature profile need to be leveled off via thermal diffusion before developed heat transfer can occur. Therefore, we also observe a nearly linear relation between the onset point $x_{\text{periodic,T}}$ and fin height h for intermediate values of h/l . Secondly, we observe that the onset point $x_{\text{periodic,T}}$ eventually becomes independent of the relative fin height h/l upon further increasing h/l . This is a result of the temperature field becoming more two-dimensional and thus independent of h/l for larger channel heights, following the flow field [15]. This second trend is, however, only visible for the lowest Prandtl number $Pr_f = 0.7$ in Figure 5. Indeed, for $Pr_f = 7$, the trend is expected to occur at much higher h/l values, outside the range considered in Figure 5. We argue that when the Prandtl number Pr_f increases, thermal diffusion becomes less important with respect to momentum diffusion so that the temperature field will become two-dimensional at larger values of h/l [15]. Anyway, both trends are further supported by the empirical correlations displayed in Figure 5, which are able to predict the data for $h/l \geq 0.16$ and $h/l \geq 0.2$ when $Pr_f = 0.7$ and $Pr_f = 7$, respectively, within a relative error of 6%.

Finally, Figure 6 displays the influence of the fin pitch-to-length ratio s/l on the onset point $x_{\text{periodic,T}}$. The influence of s/l is again well predicted by a linear relation, since the following fitted curves are accurate to within 6%: $(x_{\text{periodic,T}} - s_0)/l_1 \simeq 7.18(s/l) - 1.19$ for $Pr_f = 0.7$ and $(x_{\text{periodic,T}} - s_0)/l_1 \simeq 40.4(s/l) - 7.19$ for $Pr_f = 7$. The linearity of this relation resembles the linear trend between the onset point $x_{\text{periodic,T}}$ and relative width N_2 , which suggests that the primary influence of s/l consists of changing the transversal length over which diffusive transport must occur in the course of thermal development.

In general, from the data shown in Figures 3-6, we conclude that for air, the thermal development length $(x_{\text{periodic,T}} - s_0)$ typically remains below the streamwise length of two unit cells in offset strip fin micro- and mini-channels. Furthermore, the thermal development length for water remains smaller than 12 unit cell lengths for all cases

considered in this work. So, the short thermal development lengths are in agreement with the short flow development lengths observed in these channels [58].

We remark that, in addition to the onset point, we have also assessed the end point of the periodically developed heat transfer region in the former offset strip fin arrays. This end point $x_{\text{end},T}$ has been computed as the streamwise coordinate x_1 after which the temperature field deviates again from the periodically developed solution with more than 10% of the temperature change over the unit cell: $|T - T_{\text{dev}}|/|\nabla T \cdot \mathbf{l}_1| \geq 0.1$ for $x_1 \geq x_{\text{end},T}$. For all the computed cases in this work, this end point was found to practically coincide with the end of the fin array: $x_{\text{end},T} \simeq L_1 - s_N$.

Later, in Section 4, we will explain the observed trends for the onset point $x_{\text{periodic},T}$ from the characteristics of the quasi-developed heat transfer regime, which will be shown to cover the largest part of the development region. However, in the next sections, we first discuss the onset of developed macro-scale flow and its implications for the accuracy of our developed Nusselt number correlations.

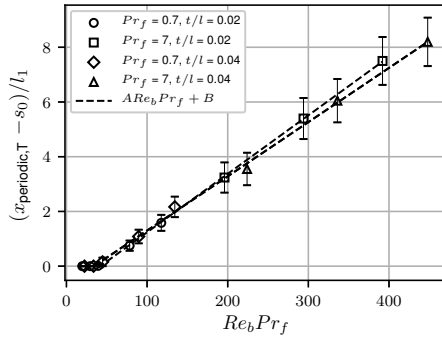


Figure 3: Influence of the Péclet number on the onset of streamwise periodically developed heat transfer, when $N_2 = 10$, $h/l = 0.12$, $s/l = 0.48$

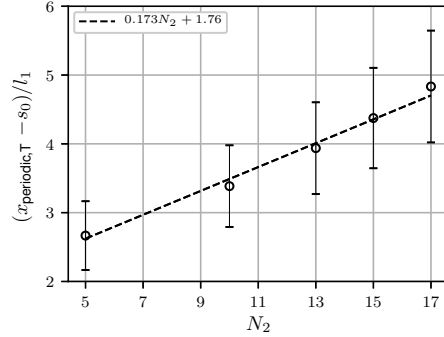


Figure 4: Influence of the channel aspect ratio on the onset of streamwise periodically developed heat transfer, when $Pr_f = 7$, $Re_b = 28$, $h/l = 0.12$, $s/l = 0.48$, $t/l = 0.02$

3.2. Region of developed macro-scale heat transfer

The heat transfer regime is considered developed from a macro-scale perspective once the macro-scale temperature profiles of the fluid and solid display a linear varia-

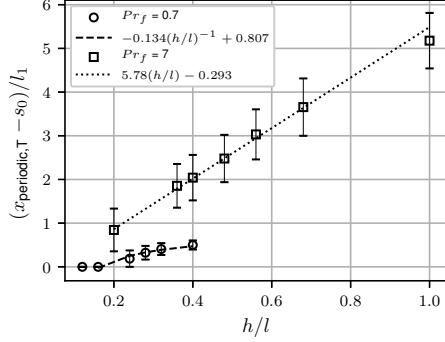


Figure 5: Influence of the fin height-to-length ratio on the onset of streamwise periodically developed heat transfer, when $Re_b l / (2L_3) = \rho_f u_b l / \mu_f = 600$, $N_2 = 10$, $s/l = 0.12$, $t/l = 0.02$

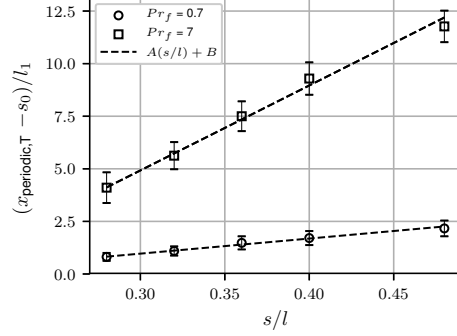


Figure 6: Influence of the fin pitch-to-length ratio on the onset of streamwise periodically developed heat transfer, when $Re_b = 192$, $N_2 = 10$, $h/l = 0.12$, $t/l = 0.04$

tion over space, at least at a distance l_1 from the side walls, where the spatial moments $\langle \gamma_f \mathbf{y} \rangle_m^f$ and $\langle \gamma_s \mathbf{y} \rangle_m^s$ are zero [33]:

$$\begin{aligned} \langle T \rangle_m^f &\simeq \langle T_{\text{dev}} \rangle_m^f \triangleq \nabla T \cdot (\mathbf{x} + \langle \gamma_f \mathbf{y} \rangle_m^f) + \langle T^* \rangle_m^f, \\ \langle T \rangle_m^s &\simeq \langle T_{\text{dev}} \rangle_m^s \triangleq \nabla T \cdot (\mathbf{x} + \langle \gamma_s \mathbf{y} \rangle_m^s) + \langle T^* \rangle_m^s. \end{aligned} \quad (9)$$

This follows directly from (8), as the gradient ∇T is constant and the spatial moments, as well as $\langle T^* \rangle_m^f$ and $\langle T^* \rangle_m^s$ are only a function of the transversal coordinate x_2 in the channel. As shown in [33], the constant macro-scale temperature gradient is determined here by the incoming heat rate $\langle q_b \delta_{bs} \rangle_m = \langle q_{fs} \delta_{fs} \rangle_m$ and the uniform macro-scale flow velocity $\langle \mathbf{u}^* \rangle_m$ in the developed region, whose unit direction is e_s :

$$\nabla \langle T \rangle_m = \nabla \langle T \rangle_m^f = \nabla \langle T \rangle_m^s = \nabla T = \frac{\langle q_b \delta_b \rangle_m}{\rho_f c_f \|\langle \mathbf{u}^* \rangle_m\|} e_s. \quad (10)$$

Strictly speaking, the linear temperature profiles (9) with the constant gradient (10) will occur at a distance l_1 after the onset of the periodically developed heat transfer, due to our choice of filter window: $\Omega_{\text{unit}}^{2 \times 2}$. Therefore, the proper definition of the region of developed macro-scale heat transfer is given by $\mathbf{x} \in \Omega_{\text{dev},T} \leftrightarrow x_1 \in (x_{\text{dev},T}, x_{\text{end},T} - l_1)$, where the onset point equals $x_{\text{dev},T} \triangleq x_{\text{periodic},T} + l_1$.

Yet, we found that the former definition is very conservative because the temperature profiles (9) appear to be reasonable approximations over a significantly larger

region in the channel than just $\Omega_{\text{dev},T}$. This is illustrated in Figure 7(a), where the non-dimensional temperature T^+ is defined as $T^+ \triangleq (T - T_{\text{in}})k_f/(q_b l)$. In this figure, we observe that even in the region where the macro-scale heat transfer regime is still developing, i.e. $\Omega_{\text{predev},T}$ where $x_1 \in (x_{\text{in}}, x_{\text{dev},T})$, the macro-scale temperature fields deviate less than 5% from the developed linear profiles (9).

According to Figure 7(b), this observation appears to be quite generally valid over a substantial range of Reynolds numbers. In particular, all our DNS results indicate that the deviations from the developed temperature profiles remain lower than 20% of the temperature difference over a single unit cell $|\nabla T \cdot l_1|$ in the region behind the first row of fins, up to the last row of the fins. On that account, we conclude that, from a practical perspective, the region of developed macro-scale heat transfer coincides with the region over which the weighted porosity ε_{fm} is independent of the streamwise coordinate x_1 , i.e. $x_1 \in (x_{\text{in}}, x_{\text{out}})$ with $x_{\text{in}} = s_0 + l_1$ and $x_{\text{out}} = L_1 - (s_N + l_1)$. Outside the former region, hence immediately near the channel inlet and outlet, the temperature field does become affected by the specific boundary conditions, as well as the presence of strong porosity gradients.

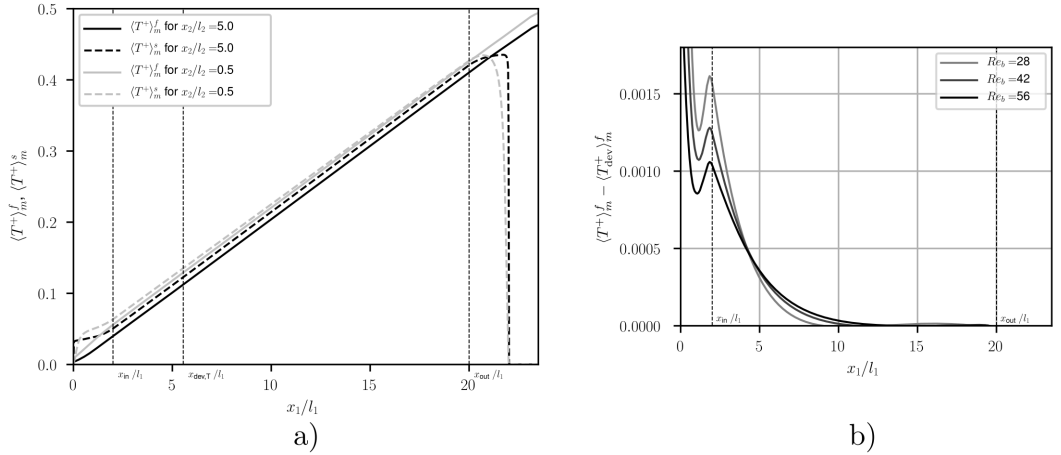


Figure 7: Intrinsic fluid and solid macro-scale temperature outside (black) and inside (grey) the side-wall region, when $Pr_f = 7$, $Re_b = 28$, $h/l = 0.12$, $s/l = 0.48$, $t/l = 0.02$, $s_0 = l_1$, $s_N = 2.5l_1$, $N_1 = 20$, and $N_2 = 10$ (a), and intrinsic fluid macro-scale temperature along the channel centerline ($x_2 = L_2/2$), when $Pr_f = 7$, $h/l = 0.12$, $s/l = 0.48$, $t/l = 0.02$, $s_0 = l_1$, $s_N = 2.5l_1$, $N_1 = 20$, and $N_2 = 10$ (b)

3.3. Accuracy of the developed Nusselt number correlation

The onset point of developed macro-scale heat transfer can also be identified as the streamwise position after which the local macro-scale heat transfer coefficients $h_{fs}(\mathbf{x})$ and $h_b(\mathbf{x})$ both become spatially constant. In particular, $h_b(\mathbf{x})$ becomes equal to the developed heat transfer coefficient h_{unit} in the center of the channel [33, 34]:

$$h_b(\mathbf{x}) \simeq h_{\text{unit}}. \quad (11)$$

The developed heat transfer coefficient h_{unit} is obtained from the developed Nusselt number: $h_{\text{unit}} \triangleq Nu_{\text{unit}} \frac{k_f}{l}$. For air ($Pr_f = 0.7$ and $k_s/k_f = 10^4$) [15], Nu_{unit} is given by the correlation

$$Nu_{\text{unit}} = c_0 + c_1 Re_l,$$

with

$$\begin{aligned} c_0 &= 6.44(h/l)^{-2} + 9.60(h/l)^{-1.24} + 24.4(s/l)^{-1.85}, \\ c_1 &= 0.112(s/l - t/l)^{-0.61}(h/l)^{-0.48}. \end{aligned} \quad (12)$$

On the other hand, for water ($Pr_f = 7$ and $k_s/k_f = 500$), it is given by

$$Nu_{\text{unit}} = d_0 + d_1 Re_l,$$

with

$$\begin{aligned} d_0 &= 3.84(h/l)^{-2} + 19.2(h/l)^{-1.39} + 22.3(s/l)^{-1.87}, \\ d_1 &= 1.26(s/l - t/l)^{-1.07}(t/l)^{0.54}(h/l)^{-0.56}. \end{aligned} \quad (13)$$

We remark that correlations (12) and (13) have an average error below 3% and 4%, respectively [15]. Their maximum error is limited to 12% and 18%, respectively.

In principle, the criterion $h_b \simeq h_{\text{unit}}$ will result in a different value for the onset point of the developed regime (11) in comparison with the former criterion (9). However, according to our numerical results, both criteria are practically identical, as Figure 8 reveals.

In Figure 8, we show the actual macro-scale heat transfer coefficient $h_b(\mathbf{x})$ along a channel at four different lateral positions with an array of 20×10 offset strip fin unit cells. In this figure, we have represented $h_b(\mathbf{x})$ by the local Nusselt number $Nu_b(\mathbf{x}) \triangleq h_b l^2 / k_f$. The two subfigures at the top correspond to an air flow, while

the two subfigures at the bottom correspond to a water flow. The considered Reynolds numbers for both fluids are relatively low ($Re_b = 42$ and $Re_b = 56$), so that the resulting Péclet numbers are low for air ($Pe \simeq 40$) and moderate for water ($Pe \simeq 400$), as of interest for many micro- and mini-channel applications [70, 7, 8].

Figure 8 illustrates that the actual macro-scale heat transfer coefficient h_b deviates less than 5% from its constant value for $x_1 \geq x_{\text{periodic,T}} = x_{\text{dev,T}} - l_1$, when viewed along the centerline $x_2 = 5l_2$ of the channel. This demonstrates that the onset point $x_{\text{periodic,T}}$ is also a good measure to indicate where the developed Nusselt number correlation becomes valid, even though $x_{\text{periodic,T}}$ is based on a criterion for the underlying temperature field instead (8). Due to numerical errors, however, the constant value of h_b in the developed value region still differs slightly from the constant value h_{unit} predicted by the correlations (12) and (13): the difference $|h_b - h_{\text{unit}}|/h_b$ may be up to 7%. These numerical errors originate mainly from the limited accuracy of the correlation, as the discretization error on h_b is around 1%.

Figure 8 also gives an impression of the typical accuracy of the developed Nusselt number correlations in the region where the flow and temperature fields are developing, at least for low to moderate Péclet numbers. In the figure, we have compared the actual local macro-scale heat transfer coefficient $h_b(\mathbf{x})$ with its local prediction $h_{\text{unit}}(\mathbf{x})$ based on the local Nusselt number $Nu_{\text{unit}}(\mathbf{x})$. Hereto, we have evaluated $Nu_{\text{unit}}(\mathbf{x})$ based on the local Reynolds number $Re_l(\mathbf{x}) \triangleq \rho_f \|\langle \mathbf{u} \rangle_m\| l / \mu_f$, for the given Prandtl number and unit cell geometry. Essentially, this means that we treat the macro-scale heat transfer regime locally as almost developed, so that the local macro-scale heat transfer coefficient is governed by the periodically developed temperature equations from [34], even when the flow is still developing. The main takeaway from this figure is that the local value $h_{\text{unit}}(\mathbf{x})$ predicted by the developed Nusselt number correlation is also quite accurate over a significant part of the developing flow and heat transfer region. After all, even upstream of the strict onset point $x_{\text{dev,T}}$, the developed Nusselt number correlations (12)-(13) predict the actual macro-scale heat transfer coefficient h_b with a mean and maximum relative error $|h_b - h_{\text{unit}}|/h_b$ of 10% and 25%, respectively. One part of the explanation is that the actual macro-scale heat transfer coefficient in the developing flow and heat transfer region only deviates between 5% and 30% from its constant

value in the developed region. However, the small error between the actual heat transfer coefficient $h_b(\boldsymbol{x})$ and its local approximation $h_{\text{unit}}(\boldsymbol{x})$ immediately upstream of the point $x_{\text{dev},T}$ can also be explained in a different way. As we will show in the next section, this error is determined by the inherent characteristics of the quasi-periodically developed heat transfer regime in $\Omega_{\text{predev},T}$.

Although Figure 8 applies to a single channel geometry and four Péclet numbers, we expect that these results are indicative for a wide range of applications [5, 6, 7, 8, 9, 10, 11, 12, 13] in which the channel height is low and the Reynolds numbers remain moderate. So, we expect that our developed heat transfer correlations can adequately model the macro-scale heat transfer regime in micro- and mini-channels with offset strip fins for most engineering purposes. Certainly, for the conditions studied here, the effects of developing heat transfer are negligible at the macro-scale level, when an accuracy level of 10% to 20% for the heat transfer coefficient is deemed acceptable. In that case, the modeling errors due to the use of developed Nusselt number correlations are also larger than the actual deviations from the developed heat transfer coefficient in the developing region anyway.

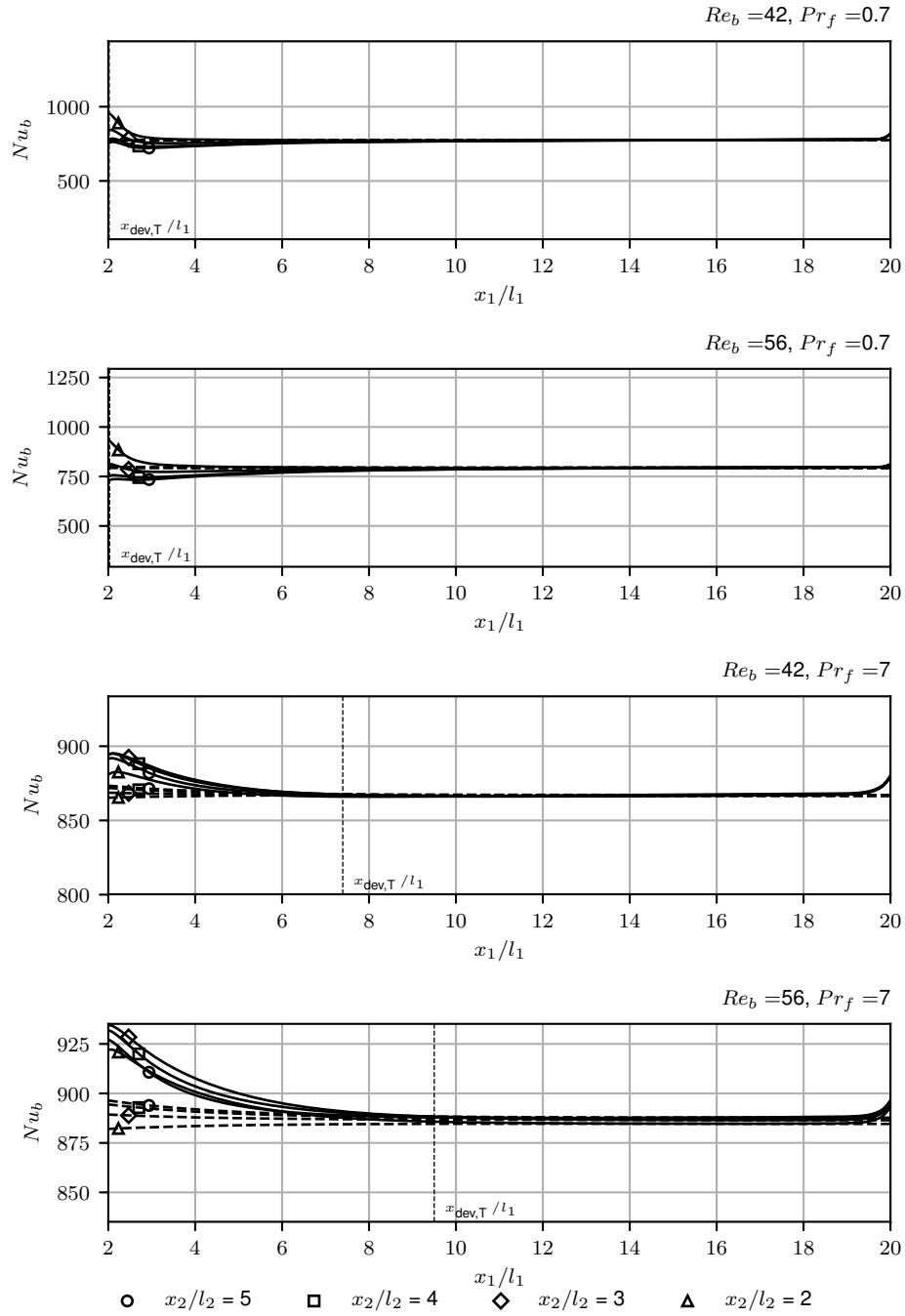


Figure 8: Macro-scale heat transfer coefficient Nu_b (full) and its prediction Nu_{unit} (dashed) by the developed correlations from [15], when $h/l = 0.12$, $s/l = 0.48$, $t/l = 0.02$, $s_0 = l_1$, $s_N = 2.5l_1$, $N_1 = 20$, and $N_2 = 10$

4. Onset of quasi-developed macro-scale heat transfer

The preceding numerical simulations have indicated that the thermal development lengths in offset strip fin micro- and mini-channels are notably short. Furthermore, they revealed that deviations from the established macro-scale temperature profiles are small, and they exposed a good accuracy of developed heat transfer correlations even upstream of the developed region. In this section, we will show that these three main observations can be attributed to the characteristics of the quasi-developed heat transfer regime, as recently described by [56]. According to our next analysis, this regime prevails over almost the entire region $\Omega_{\text{predev},T}$ where the (macro-scale) temperature field is still developing.

4.1. Onset of the quasi-periodically developed heat transfer regime

In the quasi-periodically developed heat transfer regime, the temperature field T converges asymptotically towards the developed temperature field T_{dev} from (8) along the main flow direction via a single exponential mode [56]:

$$T \simeq T_{\text{dev}} + \Theta \exp(-\lambda_T x_1). \quad (14)$$

Here, the mode's eigenvalue λ_T is a constant, while the mode's amplitude Θ is spatially periodic along the streamwise coordinate x_1 : $\Theta(\mathbf{x} + \mathbf{l}_1) = \Theta(\mathbf{x})$. We therefore define the onset point of quasi-periodically developed heat transfer, $x_{\text{quasi-periodic},T}$, as the streamwise coordinate x_1 after which the temperature field agrees with expression (14) within 10% of the temperature difference over a unit cell in the developed region, so $\Theta \exp(-\lambda_T x_1) \leq 0.1 |\nabla T \cdot \mathbf{l}_1|$ for $x_1 \geq x_{\text{quasi-periodic},T}$. The former definition of $x_{\text{quasi-periodic},T}$ is analogous to that of $x_{\text{periodic},T}$. The extent of the quasi-periodically developed heat transfer region is thus given by $x_1 \in (x_{\text{quasi-periodic},T}, x_{\text{periodic},T})$.

In figure 9, the onset point $x_{\text{quasi-periodic},T}$ has been quantified for two channel geometries and two Prandtl numbers. This figure illustrates our more general observation that for all the cases considered in this work, the onset point of the quasi-periodically developed heat transfer regime virtually coincides with the first row of the fin array. In other words, in these kinds of micro- and mini-channels, the temperature field throughout the entire array of offset strip fins can be regarded as quasi-developed, just like the

flow field [58]. Nevertheless, it is important to note that the onset point $x_{\text{quasi-periodic},T}$ in principle depends on the Prandtl number of the fluid. So, for higher Prandtl numbers than those considered in this work, one may expect the onset point $x_{\text{quasi-periodic},T}$ to be located (slightly) more downstream than the onset point of quasi-periodically developed flow $x_{\text{quasi-periodic}}$. For the low to moderate Prandtl numbers in this study, however, this spatial lagging between $x_{\text{quasi-periodic},T}$ and $x_{\text{quasi-periodic}}$ is not visible.

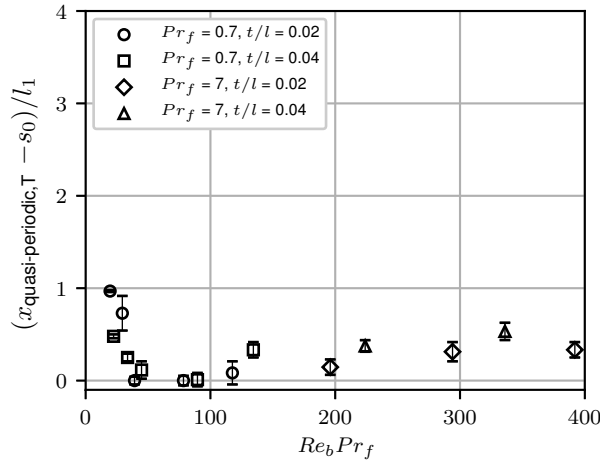


Figure 9: Influence of the Péclet number on the onset of the quasi-developed heat transfer, when $N_1 = 20$, $h/l = 0.12$, $s/l = 0.48$

4.2. Eigenvalues and perturbations for quasi-periodically developed heat transfer

Since the temperature field can be practically described as quasi-periodically developed over the entire offset strip fin array, the onset and extent of the periodically developed heat transfer regime are, in the first place, determined by the eigenvalue of the exponentially decaying mode (14). In the second place, they are also affected by the peak value of the mode's amplitude, which results from the specific inlet conditions. The former statements can be understood from the relation between the onset point of developed heat transfer $x_{\text{periodic},T}$, the eigenvalue λ_T and mode amplitude Θ ,

which follows directly from equation (14):

$$x_{\text{periodic},T} \simeq \frac{1}{\lambda_T} \ln \left(\frac{\varepsilon_{0,T}}{\varepsilon_T} \right). \quad (15)$$

In this relation, ε_T is the criterion used for defining the onset point $x_{\text{periodic},T}$. More specifically, ε_T is defined by $|T - T_{\text{dev}}|/|\nabla T \cdot \mathbf{l}_1| \leq \varepsilon_T$ for $x_1 \geq x_{\text{periodic},T}$. As explained in Section 3.1, we have adopted the criterion $\varepsilon_T = 0.1$ in this work. Further, the relative temperature difference $\varepsilon_{0,T}$ is a measure for the maximum deviation from the developed temperature profile at the onset point of the quasi-periodically developed heat transfer regime: $|T - T_{\text{dev}}|/|\nabla T \cdot \mathbf{l}_1| \leq \varepsilon_{0,T} \exp(-\lambda_T x_{\text{quasi-periodic},T})$ for $x_1 \geq x_{\text{quasi-periodic},T}$. Therefore, $\varepsilon_{0,T}$ characterizes the peak value of the mode amplitude at $x_{\text{quasi-periodic},T}$: $\varepsilon_{0,T} = \max_{\mathbf{x} \in S} |\Theta/(\nabla T \cdot \mathbf{l}_1)|$ with $S \triangleq \{\mathbf{x} | x_1 = x_{\text{quasi-periodic},T}\}$. The exact value of this factor $\varepsilon_{0,T}$, also called the *temperature perturbation size*, depends on how the temperature field becomes developed and, as such, the specific inlet conditions and channel inlet geometry. For instance, $\varepsilon_{0,T}$ is influenced by the distance s_0 between the inlet and the fin array, although it is not affected by the outlet geometry nor s_N .

From relationship (15), we learn that the relatively short thermal development lengths in offset strip fin micro- and mini-channels can be understood as a consequence of the relatively large eigenvalues λ_T of the temperature modes in these channels. Because the eigenvalues λ_T are the solutions to a periodic eigenvalue problem on a single row of the entire fin array, which is given in [56], their relatively large magnitude is an inherent property of the geometry of the offset strip fin row.

From relationship (15) we also learn that the onset point of periodically developed heat transfer will scale as $x_{\text{periodic},T} \sim 1/\lambda_T$ when the peak value of the mode amplitude has no significant effect on the logarithmic factor $\ln(\varepsilon_{0,T}/\varepsilon_T)$. As we will demonstrate next, the scaling law $x_{\text{periodic},T} \sim 1/\lambda_T$ explains well the influence of the Reynolds number, the Prandtl number and channel aspect ratio on the onset point $x_{\text{periodic},T}$.

The fact that the scaling law $x_{\text{periodic},T} \sim 1/\lambda_T$ explains the previously observed linear relation between the onset point $x_{\text{periodic},T}$ and the Reynolds number Re_b appears from the linear relation between $1/\lambda_T$ and Re_b in Figure 10. In this Figure, the linear variation of the inverse eigenvalue $1/\lambda_T$ with the Reynolds number Re_b is depicted for two channel geometries and two Prandtl numbers. The uncertainty bars on

the eigenvalues obtained through DNS indicate the possible error margins due to discretization errors and the employed least-square regression technique. The notion that $x_{\text{periodic,T}}/l_1 \sim 1/(\lambda_T l_1) \sim A Re_b + B$ for some constants A and B is also in line with our observation that the logarithmic perturbation size $\ln(\varepsilon_{0,T}/\varepsilon_T)$ remains constant to a first-order approximation over a wide range of Reynolds numbers, according to our DNS results. For instance, over the range of Reynolds numbers in Figure 10, we found that $\varepsilon_{0,T} \simeq 3.67$ when $t/l = 0.02$, and $\varepsilon_{0,T} \simeq 6.56$ when $t/l = 0.04$ with a relative error below 10%. This observation remains valid as long as the shape of the velocity profile and temperature profile at the channel inlet are kept fixed, hence independent of the Reynolds number Re_b . Strong changes in the inlet profiles could of course induce very different temperature perturbations, so that the observed similarity of the velocity and temperature profiles at different Reynolds numbers could get lost. We remark that the inversely linear relationship between the temperature eigenvalue λ_T and Reynolds number Re_b expresses a direct analogy with the quasi-periodically developed flow regime, in which the eigenvalue λ of the velocity mode is also an inversely linear function of Re_b [58].

As Figure 10 illustrates, the influence of the Prandtl number Pr_f on the eigenvalue λ_T can be captured by an inversely linear correlation in terms of the Péclet number. For both Prandtl numbers shown in Figure 10, the following correlations hold with a maximum relative error of 10%: $\lambda_T l_1 \simeq 1/(0.00812Pe + 0.0999)$ for $t/l = 0.02$, and $\lambda_T l_1 \simeq 1/(0.00810Pe + 0.0994)$ for $t/l = 0.04$. Because the temperature perturbation size $\varepsilon_{0,T}$ barely changes with the Péclet number, so that $x_{\text{periodic,T}} \sim 1/\lambda_T$, these correlations explain directly why the onset point of the periodically developed heat transfer regime $x_{\text{periodic,T}}$ scales linearly with the Péclet number for a single offset strip fin channel geometry, as we described in Section 3.1.

When we compare the eigenvalues λ_T of the temperature modes from Figure 10 with the eigenvalues λ of the velocity modes in the quasi-periodically developed flow regime [58], we find that λ_T is a factor of four to eight larger than λ when $Pr_f = 0.7$. This supports our earlier observation that the onset point $x_{\text{periodic,T}}$ is located upstream of the onset point of the periodically developed flow regime x_{periodic} when $Pr_f = 0.7$, since $x_{\text{periodic,T}}/x_{\text{periodic}} \sim \lambda/\lambda_T$, because of $x_{\text{quasi-periodic,T}} \simeq x_{\text{quasi-periodic}} \simeq s_0 + l_1$. On

the contrary, when $Pr_f = 7$, both $x_{\text{periodic},T}$ and x_{periodic} have the same order of magnitude, as λ and λ_T exhibit similar magnitudes as well.

In Figure 11, we show the dependence of the eigenvalue λ_T on the number of units cells in the lateral direction N_2 , hence the inverse channel aspect ratio L_2/L_3 , for a rather low Reynolds number $Re_b = 28$, and a small channel height $h/l = 0.12$. It can be seen that the inverse eigenvalue $1/\lambda_T$ is again a linear function of N_2 , just like the inverse eigenvalue $1/\lambda$ of the velocity modes in quasi-periodically developed flow [58]. For the data in Figure 11, we obtained the correlation $\lambda_T l_1 \simeq 1/(0.0689N_2 + 1.12)$, which is accurate within a maximum relative error of 4%. In addition, we found that $\varepsilon_{0,T} \simeq 3.33$ within an error of 10%, so that the factor $\ln(\varepsilon_{0,T}/\varepsilon_T)$ varies about 3% with N_2 . So, the logarithmic perturbation size $\ln(\varepsilon_{0,T}/\varepsilon_T)$ is virtually independent of the channel's aspect ratio. The scaling law $x_{\text{periodic},T} \sim 1/\lambda_T$ therefore recovers the correct relationship between the onset point $x_{\text{periodic},T}$ and aspect ratio as described before, i.e. $x_{\text{periodic},T} \sim 1/\lambda_T \sim AN_2 + B$, where A and B are constants.

Whereas the scaling law $x_{\text{periodic},T} \sim 1/\lambda_T$ accounts for the observed dependence of the onset point $x_{\text{periodic},T}$ on the Péclet number and the aspect ratio, it falls short of describing the influence of the fin height-to-length ratio h/l and fin pitch-to-length ratio s/l . The reason is that the latter parameters significantly affect the temperature perturbation size. According to Figure 12, the dependence of the eigenvalue λ_T on the fin height-to-length ratio h/l is described by an inversely linear relationship: $\lambda_T l_1 \simeq 1/(0.879(h/l) + 1.75)$ with an accuracy of 4%. This agrees with our expectation that the channel height h and channel width L_2 have a similar impact on the transport of thermal energy. Yet, for the data in Figure 12, we found that the temperature perturbation size satisfies $\varepsilon_{0,T} \simeq 3.55(h/l) - 0.156$ within an error of 10%, so that the factor $\ln(\varepsilon_{0,T}/\varepsilon_T)$ almost doubles over the interval $h/l \in (0.2, 1.0)$.

Similarly, the fin pitch-to-length ratio s/l has a strong influence on both the eigenvalue λ_T and induced temperature perturbation size $\varepsilon_{0,T}$. Figure 13 illustrates this for a water flow ($Pr_f = 7$) at a moderate Reynolds number $Re_b = 192$ through a compact channel with a dense array of offset strip fins: $N_2 = 10$, $h/l = 0.12$, $t/l = 0.04$ and $s/l \in (0.28, 0.48)$. It can be seen that the eigenvalue λ_T in this case varies with the fin pitch-to-length ratio s/l according to $\lambda_T l_1 \simeq 1/(37.9(s/l) - 8.91)$, within a relative

error of 5%. For the same DNS data, it was found that within 10%, the temperature perturbation size is given by $\varepsilon_{0,T} \simeq 19.8(s/l) - 4.47$. Therefore, the observed scaling of $x_{\text{periodic},T}$ with s/l in Section 3.1 is a complex interplay between the actual inlet conditions and the eigenmodes in the quasi-periodically developed heat transfer regime. The strong effect of the fin height-to-length ratio and pitch-to-length ratio on the temperature perturbations can be understood from their effect on the flow field. When the fin height or pitch increases, the flow will experience relatively less friction due to the channel walls or fin sides. In turn, perturbations in the temperature field will be more strongly advected in the streamwise direction with less dampening due to transversal diffusion since the transversal distance to the channel walls or fin sides is larger.

Finally, we illustrate the temperature modes in a typical channel geometry for three rather low Reynolds numbers in Figure 14. In this figure, the non-dimensional temperature mode is defined as $\Theta^+ \triangleq \Theta k_f / (q_b l)$. It can be recognized that the maximum of the dimensionless mode amplitude Θ^+ is inversely proportional to Reynolds number Re_b . This means that the maximum of the actual mode amplitude Θ varies inversely with the mass flow rate, and hence the developed volume-averaged velocity $\|\langle \mathbf{u}^* \rangle\|$. This, in turn, implies that the maximum of the temperature mode Θ is proportional to the temperature difference over a unit cell $|\nabla T \cdot \mathbf{l}_1|$, so that the temperature perturbation size $\varepsilon_{0,T}$ can be treated as independent of the flow rate and Reynolds number, as discussed before.

In conclusion, our observations show that the quick onset of the periodically developed heat transfer regime is mainly explained by the large magnitude of the mode eigenvalues and their scaling laws with respect to the Reynolds number, Péclet number, and aspect ratio. The mode amplitudes are of secondary importance. They account for some of the effects of the unit cell geometry and, thus, the array porosity on the development length.

4.3. Region of quasi-developed macro-scale heat transfer

Given that the heat transfer regime can be regarded as quasi-periodically developed nearly from the start of the offset strip fin array in micro- and mini-channels, also the macro-scale temperature field can be characterized as quasi-developed across most of

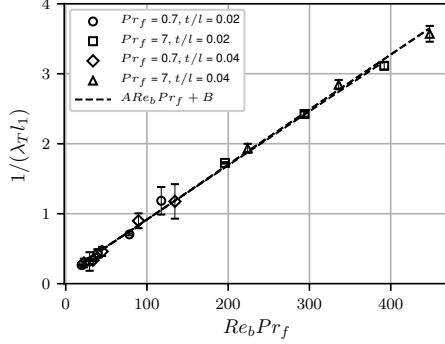


Figure 10: Influence of the Péclet number on the eigenvalue of the quasi-developed heat transfer, when $N_1 = 20$, $h/l = 0.12$, $s/l = 0.48$

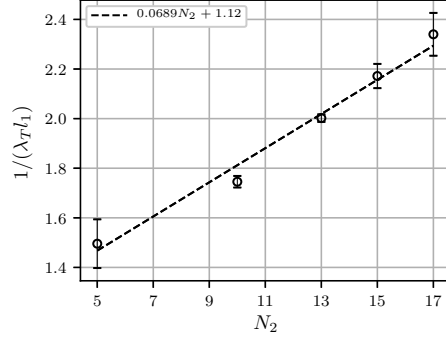


Figure 11: Influence of the channel aspect ratio on the eigenvalue of the quasi-developed heat transfer, when $Pr_f = 7$, $Re_b = 28$, $N_1 = 20$, $h/l = 0.12$, $s/l = 0.48$, $t/l = 0.02$

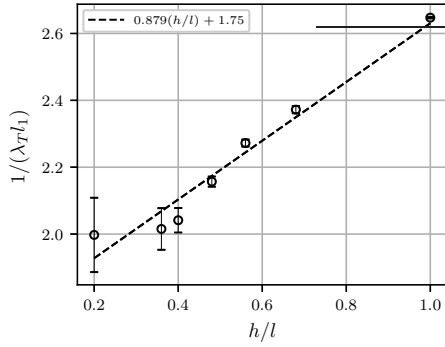


Figure 12: Influence of the fin height-to-length ratio on the eigenvalue of the quasi-developed heat transfer, when $Pr_f = 7$, $Re_b l / (2L_3) = \rho_f u_b l / \mu_f = 600$, $N_1 = 20$, $N_2 = 10$, $s/l = 0.12$, $t/l = 0.02$

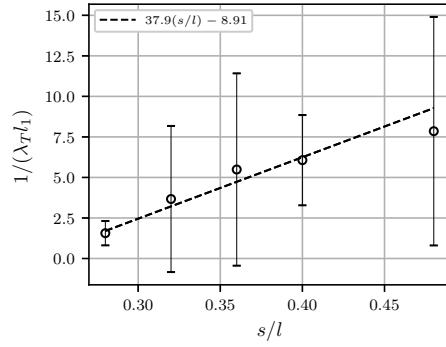


Figure 13: Influence of the fin pitch-to-length ratio on the eigenvalue of the quasi-developed heat transfer, when $Pr_f = 7$, $Re_b = 192$, $N_1 = 20$, $N_2 = 10$, $h/l = 0.12$, $t/l = 0.04$

the fin array. The small deviations from the developed macro-scale temperature profile discussed in Section 3.2 are thus primarily explained by the fast decaying temperature modes in $\Omega_{\text{predev},T}$, since the eigenvalue λ_T is quite large:

$$\begin{aligned} \langle T \rangle_m^f &\simeq \nabla T \cdot (\mathbf{x} + \langle \gamma_f \mathbf{y} \rangle_m^f) + \langle T^* \rangle_m^f + \langle \Theta \rangle_m^f \exp(-\lambda_T x_1), \\ \langle T \rangle_m^s &\simeq \nabla T \cdot (\mathbf{x} + \langle \gamma_s \mathbf{y} \rangle_m^s) + \langle T^* \rangle_m^s + \langle \Theta \rangle_m^s \exp(-\lambda_T x_1). \end{aligned} \quad (16)$$

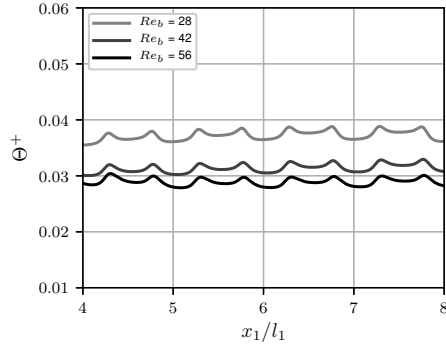


Figure 14: Temperature mode amplitude along the channel centerline ($x_2 = L_2/2, x_3 = L_3/2$), when $Pr_f = 7$, $h/l = 0.12$, $s/l = 0.48$, $t/l = 0.02$, $s_0 = l_1$, $s_N = 2.5l_1$, $N_1 = 20$, and $N_2 = 10$

Strictly speaking, the region of the quasi-developed macro-scale heat transfer regime, where the former temperature profiles (16) apply, is given by $x_1 \in (x_{\text{quasi-dev,T}}, x_{\text{dev}})$, where the onset point corresponds to $x_{\text{quasi-dev,T}} = x_{\text{quasi-periodic,T}} + l_1$. Nevertheless, in practise we may take $x_{\text{quasi-dev,T}} \simeq x_{\text{quasi-periodic,T}}$ for the same reasons as why we can take $x_{\text{dev,T}} \simeq x_{\text{periodic,T}}$.

The macro-scale temperature mode amplitudes $\langle \Theta \rangle_m^f$ and $\langle \Theta \rangle_m^s$, in the former expressions (16) for the intrinsic macro-scale temperatures are only a function of the transversal coordinate x_2 in the channel. In Figures 15 and 16, they are illustrated in their dimensionless form for the same Reynolds number, Prandtl number and geometry as in Figure 14. Their W-like shape strongly resembles the shape of the velocity modes $\langle U \rangle_m^f$ in the quasi-developed flow region because the temperature modes are advected by the same periodic flow field \mathbf{u}^* as the velocity modes, according to the eigenvalue problem from [55]. This shape reflects that the deviations from the developed macro-scale temperature profile are most pronounced at the center of the channel and at a distance of l_1 from the side walls.

Theoretically, the magnitude (or peak value) of both amplitudes $\langle \Theta \rangle_m^f$ and $\langle \Theta \rangle_m^s$ depends on the specific inlet conditions and channel inlet geometry. Nevertheless, it can be seen from Figures 15 and 16 that the influence of the Reynolds number Re_b on the shape of the macro-scale temperature modes is small. As such, their profile can be

assumed to be universal for a single channel geometry. For example, for the macro-scale temperature modes in Figures 15 and 16, we can define the following reference profile to characterize their shape at a distance l_2 away from the side walls:

$$\Theta_{\text{ref}} \triangleq \frac{q_b l}{k_f} \sin\left(\frac{2\pi}{L_2}(x_2 - L_2/4)\right). \quad (17)$$

Closer to the side walls, however, the actual profile diverges from this reference profile due to the imposed no-heat-flux boundary condition and the loss of transversal periodicity in the solid material distribution γ_s . Based on the reference profile (17), the modes for all Reynolds numbers in Figures 15 and 16 can be correlated as $\langle \Theta \rangle_m^f / \Theta_{\text{ref}} \simeq 0.940 Re_b^{-1} - 7.82e-5$ and $\langle \Theta \rangle_m^s / \Theta_{\text{ref}} \simeq 1.15 Re_b^{-1} - 0.00177$, at least within a maximum relative error of 10%. The small coefficients in these correlations verify again our observation that the thermal perturbation size $\varepsilon_{0,T}$ is approximately independent of Re_b , as discussed in Section 4.2.

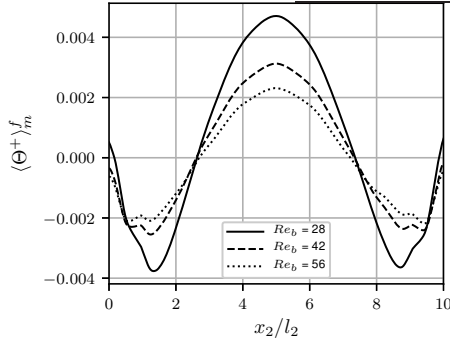


Figure 15: Influence of the Reynolds number on the intrinsic macro-scale fluid temperature mode for quasi-developed heat transfer, when $Pr_f = 7$, $N_2 = 10$, $h/l = 0.12$, $s/l = 0.48$, $t/l = 0.02$

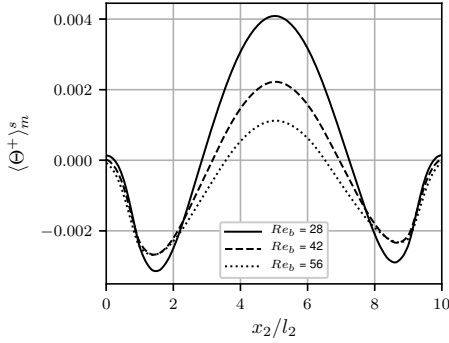


Figure 16: Influence of the Reynolds number on the intrinsic macro-scale solid temperature mode for quasi-developed heat transfer, when $Pr_f = 7$, $N_2 = 10$, $h/l = 0.12$, $s/l = 0.48$, $t/l = 0.02$

4.4. Closure for the quasi-developed heat transfer region

The relatively large eigenvalues and small induced magnitudes of the macro-scale temperature modes in the quasi-developed heat transfer region directly account for the

good accuracy of the developed Nusselt Number correlations even where the temperature field is still developing. Mathematically, this can also be understood from the asymptotically correct forms of the true macro-scale heat transfer coefficients h_{fs} and h_b in $\Omega_{\text{predev},T}$, which are given by

$$h_{fs} \simeq h_{fs,\text{dev}} + \varepsilon_{fm}^{-1} \frac{k_f \langle \mathbf{n}_{fs} \cdot \nabla \Theta_f \delta_{fs} \rangle_m}{\langle T^* \rangle_m^f - \langle T^* \rangle_m^s} \exp(-\lambda_T x_1), \quad (18)$$

and

$$h_b \simeq h_{b,\text{dev}} \left(1 - \frac{\langle \Theta \rangle_m^f - \langle \Theta \rangle_m^s}{\langle T^* \rangle_m^f - \langle T^* \rangle_m^s} \exp(-\lambda_T x_1) \right), \quad (19)$$

as it follows from (14). Here, $h_{fs,\text{dev}} \triangleq \varepsilon_{fm}^{-1} \langle \mathbf{n}_{fs} \cdot k_f \nabla T_f^* \delta_{fs} \rangle_m / (\langle T^* \rangle_m^f - \langle T^* \rangle_m^s)$ and $h_{b,\text{dev}} \triangleq \varepsilon_{fm}^{-1} \langle q_b \delta_s \rangle_m / (\langle T^* \rangle_m^f - \langle T^* \rangle_m^s)$ denote the macro-scale heat transfer coefficients in the developed region [33], of which the last one equals h_{unit} away from the channel's side walls. As a technical remark, we clarify that the former asymptotic expressions and definitions of $h_{fs,\text{dev}}$ and $h_{b,\text{dev}}$ have been obtained by neglecting the contributions from the spatial moments to the macro-scale temperature difference between the solid and fluid, since $\nabla T \cdot (\langle \gamma_f \mathbf{y} \rangle_m^f - \langle \gamma_s \mathbf{y} \rangle_m^s) \ll \langle T^* \rangle_m^f - \langle T^* \rangle_m^s$ for the double volume-averaging operator. Besides, we have $\langle \gamma_f \mathbf{y} \rangle_m^f = \langle \gamma_s \mathbf{y} \rangle_m^s = 0$ in $\Omega_{\text{predev},T} \setminus \Omega_{\text{sides}}$ anyway for the double volume-averaging operator [34]. In addition, we have neglected the contribution $-\varepsilon_{fm}^{-1} \nabla \varepsilon_{fm} \cdot k_f \nabla T / (\langle T^* \rangle_m^f - \langle T^* \rangle_m^s)$ in the definition of $h_{fs,\text{dev}}$, assuming that the porosity gradient $\nabla \varepsilon_{fm}$ in the region near the side walls is perpendicular to the main flow direction e_s .

From the asymptotic expression (19), we can determine the section $x_1 = x_h$ after which the actual heat transfer coefficient h_b agrees with the developed heat transfer coefficient h_{unit} within a relative difference ε_h . However, from our DNS experiments in Section 3.3 and in particular Figure 8, it appears that the exponential correction term on the right hand side of equation (19) adds little accuracy. This is because it decays sufficiently fast, especially when multiplied with the temperature difference $\langle T \rangle_m^f - \langle T \rangle_m^s$ to model the macro-scale interfacial heat transfer (5). This is an alternative viewpoint on why we can rely on the developed correlations for h_{unit} to model the macro-scale interfacial heat transfer h_b over nearly the entire channel, except the region near the side walls.

Although our DNS experiments have indicated that the remaining closure terms for the macro-scale energy conservation equations are completely negligible within the fin array, it is still instructive to examine their form in the quasi-developed flow and heat transfer region. The macro-scale thermal dispersion source in $\Omega_{\text{predev,T}}$ for instance is given by

$$\begin{aligned} \mathbf{D} \simeq & \mathbf{D}_{\text{dev}} + (\langle \mathbf{u}^* \Theta \rangle_m - \langle \mathbf{u}^* \rangle_m \langle \Theta \rangle_m^f) \exp(-\lambda_T x_1) \\ & + (\langle \mathbf{U} T^* \rangle_m - \langle \mathbf{U} \rangle_m \langle T^* \rangle_m^f) \exp(-\lambda x_1) \\ & + (\langle \mathbf{U} \mathbf{y} \rangle_m - \langle \mathbf{U} \rangle_m \langle \gamma_f \mathbf{y} \rangle_m^f) \cdot \nabla T \exp(-\lambda x_1). \end{aligned} \quad (20)$$

Here, $\mathbf{D}_{\text{dev}} \triangleq \langle \mathbf{u}^* T^* \rangle_m - \langle \mathbf{u}^* \rangle_m \langle T^* \rangle_m^f + \langle \mathbf{u}^* \mathbf{y} \rangle_m \cdot \nabla T - \langle \mathbf{u}^* \rangle_m \langle \gamma_f \mathbf{y} \rangle_m^f \cdot \nabla T$ represents the macro-scale thermal dispersion source in $\Omega_{\text{dev,T}}$ [33], while $\mathbf{u} = \mathbf{u}^* + \mathbf{U} \exp(-\lambda x_1)$ is the quasi-periodically developed flow field, whose mode amplitude is streamwise periodic: $\mathbf{U}(\mathbf{x}) = \mathbf{U}(\mathbf{x} + l_1)$ [54]. The first-order spatial moments of the developed velocity field $\langle \mathbf{u}^* \mathbf{y} \rangle_m$ and the mode amplitude $\langle \mathbf{U} \mathbf{y} \rangle_m$ have been notated based on the coordinate vector \mathbf{y} relative to the center of filter window, although this is technically an abuse of notation [39, 34]. From the asymptotic form of the thermal dispersion source (20), we can argue that the contribution of its divergence is indeed negligible with respect to macro-scale heat transfer from the channel's bottom: $\rho_f c_f \nabla \cdot \mathbf{D} \ll \langle q_b \delta_b \rangle_m$. The argument relies on the length-scale (or order-of-magnitude) estimates $x_1 = O(L_1)$, $x_2 = O(l_2)$, $\mathbf{u} = O(u_b)$, $T^* = O(\|\nabla T\| l_1)$, $\mathbf{y} = O(l_1)$, $\nabla T = O(q_b / \rho_f c_f u_b l_1)$, and the fact that $\langle u_2 \rangle_m = O(u_b l_2 / L_1)$ because of $\nabla \cdot \langle \mathbf{u} \rangle_m = 0$. Besides, we have $\|\mathbf{U}\| \ll u_b$ and $\nabla \Theta \ll \nabla T^*$, while the spatial moments are (approximately) perpendicular to the temperature gradient ∇T . Based on the former estimates, we find that $\rho_f c_f \nabla \cdot \mathbf{D} = O(\langle q_b \delta_b \rangle_m \langle u_2 \rangle_m / u_b) = O(\langle q_b \delta_b \rangle_m l_2 / L_1)$. Given the scale separation $l_2 \ll L_1$, and hence small lateral macro-scale velocity component $\langle u_2 \rangle_m$ [58], the macro-scale thermal dispersion is thus negligible in $\Omega_{\text{predev,T}}$.

Using the same length-scale estimates, it can analogously be shown that the divergence of the thermal tortuosity terms due to the solid-fluid interface and side-wall surfaces can be neglected in the quasi-developed flow and heat transfer region. The

exact asymptotic form of these terms is given by

$$\begin{aligned}
\langle \mathbf{n}_{fs} T_f \delta_{fs} \rangle_m &\simeq \langle \mathbf{n}_{fs} T_f^* \delta_{fs} \rangle_m + \langle \mathbf{n}_{fs} \mathbf{y} \delta_{fs} \rangle_m \cdot \nabla T \\
&\quad + \langle \mathbf{n}_{fs} \delta_{fs} \rangle_m \nabla T \cdot \mathbf{x} + \langle \mathbf{n}_{fs} \Theta_f \delta_{fs} \rangle_m \exp(-\lambda_T x_1), \\
\langle \mathbf{n} T_f \delta_{\text{sides},f} \rangle_m &\simeq \langle \mathbf{n} T_f^* \delta_{\text{sides},f} \rangle_m + \langle \mathbf{n}_{fs} \mathbf{y} \delta_{\text{sides},f} \rangle_m \cdot \nabla T \\
&\quad + \langle \mathbf{n} \delta_{\text{sides},f} \rangle_m \nabla T \cdot \mathbf{x} + \langle \mathbf{n} \Theta_f \delta_{\text{sides},f} \rangle_m \exp(-\lambda_T x_1)
\end{aligned} \tag{21}$$

where $\langle \mathbf{n}_{fs} \delta_{fs} \rangle_m = -\nabla \varepsilon_{fm}$ and $\langle \mathbf{n}_{fs} \mathbf{y} \delta_{fs} \rangle_m = -\nabla \langle \mathbf{y} \gamma_f \rangle_m$, as shown in [34].

We add that the macro-scale dispersion and tortuosity terms in the quasi-developed region can also be represented by means of an exact dispersion tensor and tortuosity tensor, as we show in Appendix A. As such, these terms can be modelled via a gradient-diffusion law, as often hypothesized in the macro-scale models for porous media, see for instance [28].

We remark that in principle, the weighting function m of the filter operator $\langle \cdot \rangle_m$ should be matched to both eigenvalues λ_T and λ , as discussed in [32, 34]. Otherwise, the exponential terms in (18)-(21) cannot be moved outside the filter operator $\langle \cdot \rangle_m$. Nevertheless, for most cases, the double volume-averaging operator (3) is accurate enough to ensure the validity of the asymptotic forms (18)-(21), especially because we have $\lambda_T l_1 \ll 1$ when the Péclet number is larger than 100 according to Figures 10-13.

Due to the high Péclet number of the fluid ($Pe \gg 1$) in most applications, we can typically neglect the thermal diffusion in the fluid. Furthermore, due to the high conductivity of the solid ($k_s/k_f \gg 100$), also the temperature gradients in the solid are typically very small. Consequently, the macro-scale energy conservation equations in $\Omega_{\text{predev},T} \cup \Omega_{\text{dev},T}$ can be simplified into

$$\begin{aligned}
\rho_f c_f \mathbf{U}_{\text{dev}} \cdot \nabla \langle T \rangle_m^f &\simeq -\langle q_b \delta_{bf} \rangle_m + k_f \langle \mathbf{n}_{fs} \cdot \nabla T_f \delta_{fs} \rangle_m, \\
0 &\simeq -\langle q_b \delta_{bs} \rangle_m - k_s \langle \mathbf{n}_{fs} \cdot \nabla T_s \delta_{fs} \rangle_m.
\end{aligned} \tag{22}$$

Conform to the preceding literature [55], $\mathbf{U}_{\text{dev}} \triangleq \langle \mathbf{u}^* \rangle_m \triangleq U_{\text{dev}}(x_2) \mathbf{e}_1$ denotes here the developed macro-scale velocity profile, which is uniform away from the side walls of the channel, as characterized in [58]. As a result, the overall macro-scale energy balance in the region $\Omega_{\text{predev},T} \cup \Omega_{\text{dev},T}$ becomes

$$\rho_f c_f \mathbf{U}_{\text{dev}} \cdot \nabla \langle T \rangle_m^f \simeq -\langle q_b \delta_b \rangle_m = -h_b \varepsilon_{fm} (\langle T \rangle_m^f - \langle T \rangle_m^s), \tag{23}$$

with $h_b \simeq h_{b,\text{dev}}$. Figure 17 illustrates the validity of this final macro-scale energy balance for a section in the developed region ($x_1 = 18l_1$) as well as one in the quasi-developed region ($x_1 = 2l_1$). In this figure, the non-dimensional macro-scale velocity, uniform heat flux and macro-scale dispersion are defined such that $U_{\text{dev}}^+ \triangleq U_{\text{dev}}/u_b$, $q_b^+ \triangleq q_b/q_b = 1$ and $D^+ \triangleq D(q_b l_1)/(k_f u_b)$, while ∇ and δ_b denote the dimensionless gradient operator and Diract surface operator based on the reference length l_1 . The main takeaway is that according to the final macro-scale energy balance (23), the developed heat transfer coefficient $h_{b,\text{dev}}$ is the only relevant closure coefficient required to reconstruct the macro-scale temperature profiles of the fluid and solid over almost the entire channel. Although the former heat transfer coefficient is completely known in the core of the channel, where it becomes uniform (i.e. $h_{b,\text{dev}} = h_{b,\text{unit}}$), its spatial behavior closer to the side walls has not yet been investigated. This will be the topic of the next section.

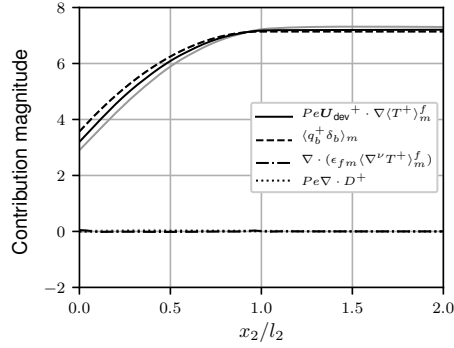


Figure 17: Macro-scale energy balance along the channel width at $x_1 = 18l_1$ (black) and $x_1 = 2l_1$ (grey), when $Re_b = 28$, $Pr_f = 7$, $h/l = 0.12$, $s/l = 0.48$, $t/l = 0.02$, $s_0 = l_1$, $s_N = 2.5l_1$, $N_1 = 20$, and $N_2 = 10$

5. Influence of the side-wall region on macro-scale heat transfer

Within a certain distance $l_{\text{sides,T}}$ from the channel side walls in the developed heat transfer region $\Omega_{\text{dev,T}}$, the streamwise periodic temperature field T^* will be no longer periodic along the transversal direction e_2 . This is a consequence of the no-heat-flux condition at the channel boundary Γ_{sides} , and the fact that the velocity field loses its transversal periodicity close to side walls, due to the no-slip condition at Γ_{sides} [58]. For our final macro-scale model (23), this implies that macro-scale heat transfer coefficient h_b in $\Omega_{\text{dev,T}}$ will vary with the coordinate x_2 near the side walls, since $\langle T^* \rangle_m^f$ and $\langle T^* \rangle_m^s$ are no longer spatially constant in that region. In order to specify the developed macro-scale heat transfer coefficient $h_{b,\text{dev}}$ in $\Omega_{\text{dev,T}}$, the profile of the temperature difference $\langle T \rangle_m^f - \langle T \rangle_m^s \simeq \langle T^* \rangle_m^f - \langle T^* \rangle_m^s$ within a distance $l_{\text{sides,T}}$ from the side walls in $\Omega_{\text{dev,T}}$ thus needs to be known.

According to our DNS data, the distance $l_{\text{sides,T}}$ is smaller than the lateral size l_2 of the unit cell, when the width of the channel is sufficiently large to allow for transversal periodicity of the velocity field. Consequently, the side-wall region where the heat transfer coefficient $h_{b,\text{dev}}$ varies with x_2 practically corresponds to $\Omega_{\text{sides,T}} = \{\mathbf{x} \in \Omega | x_2 \in (0, l_2) \cup (L_2 - l_2, L_2)\}$, which is the region where the lateral porosity gradient $d\varepsilon_{fm}/dx_2$ is nonzero. Conversely, the region where the heat transfer coefficient and other macro-scale closure terms are uniform, is given by $\Omega_{\text{uniform,T}} = \{\mathbf{x} \in \Omega | x_1 \in (x_{\text{dev,T}}, x_{\text{out}}), x_2 \in (l_2, L_2 - l_2)\}$.

To model the macro-scale heat transfer coefficient $h_{b,\text{dev}}$ in $\Omega_{\text{sides,T}} \cap \Omega_{\text{dev,T}}$, we represent the profile of the macro-scale temperature difference in this region by the following shape function ξ_T :

$$\xi_T(x_2) \triangleq \frac{\left(\langle T \rangle_m^f - \langle T \rangle_m^s \right) \Big|_{x_2}}{\left(\langle T \rangle_m^f - \langle T \rangle_m^s \right) \Big|_{x_2=l_2}}. \quad (24)$$

The non-dimensional parameter ξ_T is essentially a closure variable that maps the local macro-scale temperature difference between the fluid and solid to its uniform value outside the side-wall region. The variation of ξ_T with the coordinate x_2 perpendicular to each side wall is illustrated in Figure 18. For the data considered in Figure 18, we

find that ξ_T can be approximated by a linear profile within a maximum relative error of 5%:

$$\xi_T(x_2) \simeq \begin{cases} 1 - \kappa(x_2 - l_2) & \text{for } x_2 \in (0, l_2), \\ 1 & \text{for } x_2 \in (l_2, L_2 - l_2), \\ 1 - \kappa'(L_2 - x_2 - l_2) & \text{for } x_2 \in (L_2 - l_2, L_2). \end{cases} \quad (25)$$

The linear shape function ξ_T is then determined by the constant slopes κ and κ' at each side wall of the channel, which depends on the Reynolds number, the material properties, and fin-row geometry. Although the slopes κ and κ' of the linear profile do not necessarily have to be equal because of the asymmetric shape of the offset strip fins, we did find that the assumption $\kappa \simeq \kappa'$ is justified for all of the investigated cases. For example, the following correlations capture the data of κ and κ' within a relative error of 1% for two channel geometries with $N_2 = 10$, $h/l = 0.12$, $s/l = 0.48$, $Pr_f = 0.7$ and $Re_b \in (28, 192)$: $\kappa \simeq 2.23e-4Re_b + 0.291$ when $t/l = 0.02$ and $\kappa \simeq 3.64e-4Re_b + 0.351$ when $t/l = 0.04$.

By definition, the shape function ξ_T can be employed to model the local value of the macro-scale heat transfer coefficient h_b from its developed prediction h_{unit} :

$$h_{b,\text{dev}} = \xi_T^{-1} h_{\text{unit}}. \quad (26)$$

The macro-scale heat transfer coefficient h_{unit} can be computed from the developed Nusselt number correlation (11) based on the uniform developed macro-scale velocity outside the side-wall region, i.e. $\langle \mathbf{u}^* \rangle_m = Ue_1$ at $x_2 = l_2$. Just like the macro-scale velocity profile ξ in the side-wall region, also the temperature profile ξ_T can be determined by resolving the flow and temperature field on an extended unit cell, as suggested in [58]. Such an extended unit cell consists of one unit cell in $\Omega_{\text{sides,T}}$ and another adjacent unit cell in $\Omega_{\text{uniform,T}}$, as the width of the side-wall region equals l_2 .

In Figure 19, we have illustrated the accuracy of our linear model (25) for the developed heat transfer coefficient (26) in the side-wall region. Hereto, we compared the predicted value for $h_{b,\text{dev}}$ according to our linear model (26) with its actual value, which we computed from definition (7). Both the predicted and actual values have been represented in the form of a dimensionless Nusselt number: $Nu_{b,\text{dev}} \triangleq h_{b,\text{dev}} l^2 / k_f$.

According to Figure 19, the inexact linear expressions for ξ_T result in a relative mean and maximum error of 5% and 11% in $\Omega_{\text{sides},T} \cap \Omega_{\text{dev},T}$.

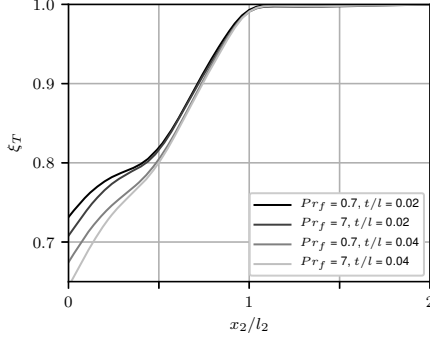


Figure 18: Macro-scale temperature difference profile in the side-wall region, when $Re_b l / (2L_3) = \rho_f u_b l / \mu_f = 100$, $N_2 = 10$, $h/l = 0.12$, $s/l = 0.48$

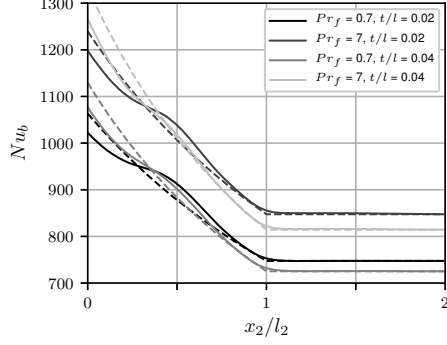


Figure 19: Macro-scale heat transfer coefficient $Nu_{b,\text{dev}}$ (full) and its prediction $\xi_T^{-1} Nu_{\text{unit}}$ (dashed) by the developed correlation from [15], when $Re_b l / (2L_3) = \rho_f u_b l / \mu_f = 100$, $N_2 = 10$, $h/l = 0.12$, $s/l = 0.48$

Finally, we add that the macro-scale temperature profile ξ_T also allows us to determine the effective boundary conditions for the macro-scale fluid temperature governed by equations (22). At least, this is true when the conductivity of the solid material is so high that the temperature in the solid region Ω_s is virtually constant, as we then have $\mathbf{n} \cdot \nabla \langle T \rangle_m^f \gg \mathbf{n} \cdot \nabla \langle T \rangle_m^s$, and thus

$$\mathbf{n} \cdot \nabla \langle T \rangle_m^f \simeq \mathbf{n} \cdot \nabla \xi_T (\langle T \rangle_m^f - \langle T \rangle_m^s) \Big|_{x_2=l_2} = -\kappa (\langle T \rangle_m^f - \langle T \rangle_m^s) \Big|_{x_2=l_2}, \quad (27)$$

$$\mathbf{n} \cdot \nabla \langle T \rangle_m^s \simeq 0,$$

for $\mathbf{x} \in \Gamma_{\text{sides}} \cap \Omega_{\text{dev},T}$. Consequently, the constant $(k_f \kappa)$ can be interpreted as an effective heat transfer coefficient relating the effective macro-scale heat flux at the side wall of the channel to the uniform macro-scale temperature difference just outside the side-wall region.

6. Conclusion

In this work, we have presented a macro-scale description of the developed and quasi-developed heat transfer regimes in micro- and mini-channels with arrays of periodic offset strip fins, subject to a uniform heat flux. The theoretical framework has been supported by direct numerical simulations of the developing temperature and flow fields in typical channel geometries. Both air and water flows have been considered for Reynolds numbers ranging from 28 to 1224. The macro-scale temperature fields have been calculated by repeated volume-averaging of the obtained temperature fields over each local unit cell in the channel.

We observed that the onset point of the developed macro-scale heat transfer regime scales linearly with the Péclet number for a given offset strip fin channel geometry. Yet, for the cases considered in this work, the thermal development length remains limited with respect to the total length of the array used in typical micro- and mini-channel applications. Particularly for air, the macro-scale temperature field can be considered developed after two unit cells in the offset strip fin array. Consequently, the developed Nusselt number correlations from our previous work are able to accurately model the macro-scale heat transfer coefficient throughout almost the entire channel. They predict the macro-scale temperature difference between the fluid and solid material near the channel inlet within a mean relative error of 10%.

Similar to the macro-scale flow field, the macro-scale temperature field becomes quasi-developed virtually after the first unit cell in the fin array for all the cases in this work. So, the macro-scale temperature field in the region immediately upstream of the developed region is characterized by a single dominant mode, which decays exponentially along the main flow direction. The relatively large eigenvalues of this mode explain the quick onset of the developed heat transfer regime, as well as the scaling of its onset point with respect to the Reynolds number, Péclet number and aspect ratio. Moreover, the large eigenvalues are directly responsible for the good accuracy of the developed heat transfer (or Nusselt number) correlations in the developing region. The small mode amplitudes still account for some of the secondary effects of the unit cell geometry on the development length.

Finally, we have empirically shown that the influence of the channel's side walls on the macro-scale heat transfer coefficient can be captured by a shape function, which varies linearly with the distance from the side walls to a first approximation. Through this shape function, the local macro-scale heat transfer coefficient in the side-wall region can be modeled with a mean and maximum error of 5% and 11%, according to our data.

7. Contributions

The macro-scale description based on the double volume-averaging operation and the validation of its computational framework were carried out by G. Buckinx. G. Buckinx formulated the theoretical framework and modeling equations for the quasi-developed macro-scale heat transfer regime. A. Vangeffelen carried out all numerical heat transfer simulations and post-processing calculations. The results were interpreted by A. Vangeffelen, with input from G. Buckinx regarding the existing literature. The paper was written by A. Vangeffelen and G. Buckinx, with input from C. De Servi, M. R. Vetrano, and M. Baelmans.

8. Acknowledgements

The work documented in this paper was funded by the Flemish Institute for Technological Research (VITO) through the Ph.D. grant 1810603 of A. Vangeffelen, and by the Research Foundation — Flanders (FWO) through the post-doctoral project grant 12Y2919N of G. Buckinx. The VSC (Flemish Supercomputer Center), funded by the Research Foundation - Flanders (FWO) and the Flemish Government, supplied the resources and services used in this work.

Appendix A. Closure problem for the quasi-periodically developed heat transfer regime under a uniform heat flux

Appendix A.1. Closure for the periodically developed region

If we propose the closure mapping

$$T_f^* = \psi_f \cdot \nabla \mathbf{T}, \quad T_s^* = \psi_s \cdot \nabla \mathbf{T}, \quad (\text{A.1})$$

and substitute this mapping in the periodic temperature equations for the periodically developed heat transfer regime under a uniform heat flux [15], we obtain the following problem for the closure variable ψ in the developed heat transfer region:

$$\begin{aligned} \rho_f c_f \mathbf{u}_f^* \cdot \nabla \psi_f + \rho_f c_f \mathbf{u}_f^* &= k_f \nabla^2 \psi_f && \text{in } \Omega_f, \\ 0 &= k_s \nabla^2 \psi_s && \text{in } \Omega_s, \\ \psi(\mathbf{x} + \mathbf{I}_1) &= \psi(\mathbf{x}), \\ -\mathbf{n} \cdot k_f (\nabla \psi_f + \mathbf{I}) &= -\rho_f c_f \mathbf{U}_{\text{dev}} / \langle \delta_b \rangle_m && \text{in } \Gamma_{bf}, \\ -\mathbf{n} \cdot k_s (\nabla \psi_s + \mathbf{I}) &= -\rho_f c_f \mathbf{U}_{\text{dev}} / \langle \delta_b \rangle_m && \text{in } \Gamma_{bs}, \\ -\mathbf{n} \cdot (\nabla \psi + \mathbf{I}) &= 0 && \text{in } \Gamma_t \cup \Gamma_{\text{sides}}, \\ \psi_f &= \psi_s && \text{in } \Gamma_{fs}, \\ -\mathbf{n}_{fs} \cdot k_f (\nabla \psi_f + \mathbf{I}) &= -\mathbf{n}_{fs} \cdot k_s (\nabla \psi_s + \mathbf{I}) && \text{in } \Gamma_{fs}. \end{aligned} \quad (\text{A.2})$$

Through the closure mapping (A.1), the gradients of the macro-scale temperatures in the fluid and solid given by (9) can be mapped to the constant temperature gradient in the developed regime: $\nabla \langle T \rangle_m^f = \mathbf{B}_{fm} \cdot \nabla \mathbf{T}$ and $\nabla \langle T \rangle_m^s = \mathbf{B}_{sm} \cdot \nabla \mathbf{T}$. The mapping tensors are defined as $\mathbf{B}_{fm} \triangleq \mathbf{I} + \nabla \langle \gamma_f \mathbf{y} \rangle_m^f + \nabla \langle \psi \rangle_m^f$ and $\mathbf{B}_{sm} \triangleq \mathbf{I} + \nabla \langle \gamma_s \mathbf{y} \rangle_m^s + \nabla \langle \psi \rangle_m^s$. Outside the side-wall region, both \mathbf{B}_{fm} and \mathbf{B}_{sm} become equal to the identity tensor \mathbf{I} .

Consequently, the closure problem (A.2) allows us to express all closure terms for the macro-scale temperature equations in terms of the macro-scale temperature gradients $\nabla \langle T \rangle_m^f$ and $\nabla \langle T \rangle_m^s$. For the macro-scale interfacial heat transfer, we obtain for instance

$$\langle q_{fs} \delta_{fs} \rangle_m = -\mathbf{K}_{fs,\text{dev}}^f \cdot \nabla \langle T \rangle_m^f = -\mathbf{K}_{fs,\text{dev}}^s \cdot \nabla \langle T \rangle_m^s \quad (\text{A.3})$$

with

$$\begin{aligned}\mathbf{K}_{fs,\text{dev}}^f &\triangleq k_f \langle \mathbf{n}_{fs} \cdot (\nabla \psi_f + \mathbf{I}) \delta_{fs} \rangle_m \cdot \mathbf{B}_{fm}^{-1}, \\ \mathbf{K}_{fs,\text{dev}}^s &\triangleq k_s \langle \mathbf{n}_{fs} \cdot (\nabla \psi_s + \mathbf{I}) \delta_{fs} \rangle_m \cdot \mathbf{B}_{sm}^{-1}.\end{aligned}\quad (\text{A.4})$$

Likewise, the thermal dispersion source can be written as

$$\mathbf{D} = \mathbf{K}_{d,\text{dev}} \cdot \nabla \langle T \rangle_m^f, \quad (\text{A.5})$$

with the developed dispersion tensor defined as

$$\mathbf{K}_{d,\text{dev}} \triangleq (\langle \mathbf{u}^* \psi_f \rangle_m - \varepsilon_{fm} \langle \mathbf{u}^* \rangle_m^f \langle \psi_f \rangle_m^f + \langle \mathbf{u}^* \mathbf{y} \rangle_m - \langle \mathbf{u}^* \rangle_m \langle \gamma_f \mathbf{y} \rangle_m^f) \cdot \mathbf{B}_{fm}^{-1}. \quad (\text{A.6})$$

Lastly, the thermal tortuosity can be represented as

$$\langle \mathbf{n}_{fs} T_f \delta_{fs} \rangle_m = \mathbf{K}_{t,\text{dev}} \cdot \nabla \langle T \rangle_m^f, \quad (\text{A.7})$$

with the developed tortuosity tensor defined as

$$\mathbf{K}_{t,\text{dev}} \triangleq (\langle \mathbf{n}_{fs} \psi_f \delta_{fs} \rangle_m + \langle \mathbf{n}_{fs} \mathbf{y} \delta_{fs} \rangle_m + \langle \mathbf{n}_{fs} \delta_{fs} \rangle_m \mathbf{x}) \cdot \mathbf{B}_{fm}^{-1}. \quad (\text{A.8})$$

A similar representation of the tortuosity terms due to the channel's side walls may be readily deduced.

Appendix A.2. Closure for the quasi-periodically developed region

If we propose the closure mapping

$$\Theta_f = \Psi_f \cdot \nabla T, \quad \Theta_s = \Psi_s \cdot \nabla T, \quad (\text{A.9})$$

and substitute this mapping in the eigenvalue problem for the quasi-periodically developed heat transfer regime under a uniform heat flux [56], we obtain the following problem for the closure variable Ψ in the quasi-developed region:

$$\begin{aligned}\rho_f c_f \mathbf{u}_f^* \cdot (\nabla \Psi_f - \lambda_T \Psi_f) &= k_f \nabla^2 \Psi_f - (2k_f \nabla \Psi_f) \cdot \lambda_T + k_f \Psi_f \lambda_T^2 && \text{in } \Omega_f, \\ 0 &= k_s \nabla^2 \Psi_s - (2k_s \nabla \Psi_s) \cdot \lambda_T + k_s \Psi_s \lambda_T^2 && \text{in } \Omega_s, \\ \Psi(\mathbf{x} + l_1) &= \Psi(\mathbf{x}), \\ -\mathbf{n} \cdot (\nabla \Psi - \lambda_T \Psi) &= 0 && \text{in } \Gamma_b \cup \Gamma_t \cup \Gamma_{\text{sides}}, \\ \Psi_f &= \Psi_s && \text{in } \Gamma_{fs}, \\ -\mathbf{n}_{fs} \cdot k_f (\nabla \Psi_f - \lambda_T \Psi_f) &= -\mathbf{n}_{fs} \cdot k_s (\nabla \Psi_s - \lambda_T \Psi_s) && \text{in } \Gamma_{fs}.\end{aligned}\quad (\text{A.10})$$

In the former closure problem, the eigenvector $\lambda_T \triangleq \lambda_T e_s$ has a different sign than in the original eigenvalue problem from [56]. To find a unique solution for the closure variable Ψ , its averaged value over a transversal row of the array may be imposed:

$$\langle \Psi \rangle_{\text{row}} \cdot e_s = \Psi_0. \quad (\text{A.11})$$

Here, the row-averaging operator $\langle \cdot \rangle_{\text{row}}$ is defined as in [55], and the scalar Ψ_0 determines the temperature perturbation size $\epsilon_{0,T}$.

The solution to the closure problem (A.10) enables us again to express all closure terms in terms of the macro-scale temperature gradients $\nabla \langle T \rangle_m^f$ and $\nabla \langle T \rangle_m^s$. The macro-scale interfacial heat transfer in the quasi-developed region is for instance given by

$$\langle q_{fs} \delta_{fs} \rangle_m = -\mathbf{K}_{fs,\text{quasi-dev}}^f \cdot \nabla \langle T \rangle_m^f = -\mathbf{K}_{fs,\text{quasi-dev}}^s \cdot \nabla \langle T \rangle_m^s \quad (\text{A.12})$$

with

$$\begin{aligned} \mathbf{K}_{fs,\text{quasi-dev}}^f &\triangleq \mathbf{K}_{fs,\text{dev}}^f + k_f \langle \mathbf{n}_{fs} \cdot (\nabla \Psi_f - \lambda_T \Psi_f) \delta_{fs} \rangle_m \cdot \mathbf{B}_{fm}^{-1} \exp(-\lambda_T \cdot \mathbf{x}), \\ \mathbf{K}_{fs,\text{quasi-dev}}^s &\triangleq \mathbf{K}_{fs,\text{dev}}^s + k_s \langle \mathbf{n}_{fs} \cdot (\nabla \Psi_s - \lambda_T \Psi_s) \delta_{fs} \rangle_m \cdot \mathbf{B}_{sm}^{-1} \exp(-\lambda_T \cdot \mathbf{x}). \end{aligned} \quad (\text{A.13})$$

Further, the thermal dispersion source is given by

$$\mathbf{D} = \mathbf{K}_{d,\text{quasi-dev}} \cdot \nabla \langle T \rangle_m^f, \quad (\text{A.14})$$

where the thermal dispersion tensor in the quasi-developed region is defined as

$$\begin{aligned} \mathbf{K}_{d,\text{quasi-dev}} &\triangleq \mathbf{K}_{d,\text{dev}} + [(\langle \mathbf{u}^* \Psi_f \rangle_m - \langle \mathbf{u}^* \rangle_m \langle \Psi_f \rangle_m^f) \exp(-\lambda_T \cdot \mathbf{x}) \\ &\quad + (\langle \mathbf{U} \psi_f \rangle_m - \langle \mathbf{U} \rangle_m \langle \psi_f \rangle_m^f) \\ &\quad + \langle \mathbf{U} \mathbf{y} \rangle_m - \langle \mathbf{U} \rangle_m \langle \gamma_f \mathbf{y} \rangle_m^f] \cdot \mathbf{B}_{fm}^{-1}. \end{aligned} \quad (\text{A.15})$$

We remark that the velocity fields \mathbf{U} and \mathbf{u}^* can be further related to the (uniform) macro-scale velocity $\mathbf{U}_{\text{dev}} \triangleq \langle \mathbf{u}^* \rangle_m$ in the quasi-developed flow region via the closure problems presented in [55].

Analogously, we can express the thermal tortuosity due to the fluid-solid interface as

$$\langle \mathbf{n}_{fs} T_f \delta_{fs} \rangle_m = \mathbf{K}_{t,\text{quasi-dev}} \cdot \nabla \langle T \rangle_m^f, \quad (\text{A.16})$$

by defining the thermal tortuosity tensor in the quasi-developed region as

$$\mathbf{K}_{t,\text{quasi-dev}} \triangleq \mathbf{K}_{t,\text{dev}} + \langle \mathbf{n}_{fs} \boldsymbol{\Psi}_f \delta_{fs} \rangle_m \cdot \mathbf{B}_{fm}^{-1} \exp(-\boldsymbol{\lambda}_T \cdot \mathbf{x}). \quad (\text{A.17})$$

Finally, we can also obtain a relationship between the deviation parts of the fluid and solid temperature on one hand, and the macro-scale temperature gradients on the other hand:

$$\begin{aligned} \tilde{T}_f &= \left(\tilde{\psi}_f - \langle \gamma_f \mathbf{y} \rangle_m^f + \tilde{\Psi}_f \exp(-\boldsymbol{\lambda}_T \cdot \mathbf{x}) \right) \cdot \mathbf{B}_{fm}^{-1} \cdot \nabla \langle T \rangle_m^f, \\ \tilde{T}_s &= \left(\tilde{\psi}_s - \langle \gamma_s \mathbf{y} \rangle_m^s + \tilde{\Psi}_s \exp(-\boldsymbol{\lambda}_T \cdot \mathbf{x}) \right) \cdot \mathbf{B}_{sm}^{-1} \cdot \nabla \langle T \rangle_m^s. \end{aligned} \quad (\text{A.18})$$

Here, the deviation operator is defined as $\tilde{\phi} \triangleq \phi - \langle \phi \rangle_m^f \gamma_f - \langle \phi \rangle_m^s \gamma_s$. The former temperature deviation parts (A.18) are not of interest for this work because we rely on the exact definitions of the closure terms. Nevertheless, they play an important role in the available closure problems for porous media, see for instance [28]. A major difference is that those closure problems for porous media only rely on periodic closure variables, whereas our result (A.18) shows that actually exponentially decaying closure variables are inherently required to obtain exact closure for the quasi-developed heat transfer regime.

References

- [1] S. Kandlikar, S. Garimella, D. Li, S. Colin, M. R. King, Heat transfer and fluid flow in minichannels and microchannels, Elsevier, 2005.
- [2] W. A. Khan, J. Culham, M. Yovanovich, The role of fin geometry in heat sink performance, *Journal of Electronic Packaging* 128 (4) (2006) 324–330.
- [3] T. İzci, M. Koz, A. Koşar, The effect of micro pin-fin shape on thermal and hydraulic performance of micro pin-fin heat sinks, *Heat Transfer Engineering* 36 (17) (2015) 1447–1457.
- [4] D. Yang, Z. Jin, Y. Wang, G. Ding, G. Wang, Heat removal capacity of laminar coolant flow in a micro channel heat sink with different pin fins, *International Journal of Heat and Mass Transfer* 113 (2017) 366–372.
- [5] A. V. Bapat, S. G. Kandlikar, Thermohydraulic performance analysis of off-set strip fin microchannel heat exchangers, in: *International Conference on Nanochannels, Microchannels, and Minichannels*, Vol. 47608, 2006, pp. 347–353.
- [6] C.-Y. Yang, C.-T. Yeh, W.-C. Liu, B.-C. Yang, Advanced micro-heat exchangers for high heat flux, *Heat transfer engineering* 28 (8-9) (2007) 788–794.
- [7] F. Hong, P. Cheng, Three dimensional numerical analyses and optimization of offset strip-fin microchannel heat sinks, *International Communications in Heat and Mass Transfer* 36 (7) (2009) 651–656.
- [8] K. H. Do, B.-I. Choi, Y.-S. Han, T. Kim, Experimental investigation on the pressure drop and heat transfer characteristics of a recuperator with offset strip fins for a micro gas turbine, *International Journal of Heat and Mass Transfer* 103 (2016) 457–467.
- [9] T. Nagasaki, R. Tokue, S. Kashima, Y. Ito, Conceptual design of recuperator for ultramicro gas turbine, in: *Proceedings of the International Gas Turbine Congress*, Citeseer, 2003, pp. 2–7.

- [10] Y. Yang, Y. Li, B. Si, J. Zheng, Heat transfer performances of cryogenic fluids in offset strip fin-channels considering the effect of fin efficiency, *International Journal of Heat and Mass Transfer* 114 (2017) 1114–1125.
- [11] Q. Jiang, M. Zhuang, Z. Zhu, J. Shen, Thermal hydraulic characteristics of cryogenic offset-strip fin heat exchangers, *Applied Thermal Engineering* 150 (2019) 88–98.
- [12] M. Yang, X. Yang, X. Li, Z. Wang, P. Wang, Design and optimization of a solar air heater with offset strip fin absorber plate, *Applied Energy* 113 (2014) 1349–1362.
- [13] K. Pottler, C. M. Sippel, A. Beck, J. Fricke, Optimized finned absorber geometries for solar air heating collectors, *Solar Energy* 67 (1-3) (1999) 35–52.
- [14] A. Vangeffelen, G. Buckinx, M. R. Vetrano, M. Baelmans, Friction factor for steady periodically developed flow in micro-and mini-channels with arrays of offset strip fins, *Physics of Fluids* 33 (10) (2021) 103610.
- [15] A. Vangeffelen, G. Buckinx, C. De Servi, M. R. Vetrano, M. Baelmans, Nusselt number for steady periodically developed heat transfer in micro-and mini-channels with arrays of offset strip fins subject to a uniform heat flux, *International Journal of Heat and Mass Transfer* 195 (2022) 123145. doi:<https://doi.org/10.1016/j.ijheatmasstransfer.2022.123145>.
- [16] D. B. Tuckerman, R. F. W. Pease, High-performance heat sinking for vlsi, *IEEE Electron device letters* 2 (5) (1981) 126–129.
- [17] R. Shah, A. London, *Laminar Flow Forced Convection in Ducts*, Vol. 1, Elsevier, 1978.
- [18] A. Renfer, M. K. Tiwari, R. Tiwari, F. Alfieri, T. Brunswiler, B. Michel, D. Poulikakos, Microvortex-enhanced heat transfer in 3d-integrated liquid cooling of electronic chip stacks, *International Journal of Heat and Mass Transfer* 65 (2013) 33–43.

- [19] G. Xia, Z. Chen, L. Cheng, D. Ma, Y. Zhai, Y. Yang, Micro-piv visualization and numerical simulation of flow and heat transfer in three micro pin-fin heat sinks, *International Journal of Thermal Sciences* 119 (2017) 9–23.
- [20] L.-z. Zhang, Z.-y. Chen, Convective heat transfer in cross-corrugated triangular ducts under uniform heat flux boundary conditions, *International Journal of Heat and Mass Transfer* 54 (1-3) (2011) 597–605.
- [21] J. Gong, J. Onishi, A. He, Y. Kametani, Y. Hasegawa, N. Shikazono, Heat transfer enhancement and pressure loss in a plate-fin heat exchanger with v-shaped oblique wavy surface, *International Journal of Heat and Mass Transfer* 161 (2020) 120263.
- [22] A. Priyam, P. Chand, Thermal and thermohydraulic performance of wavy finned absorber solar air heater, *Solar Energy* 130 (2016) 250–259.
- [23] D. Liang, G. He, W. Chen, Y. Chen, M. K. Chyu, Fluid flow and heat transfer performance for micro-lattice structures fabricated by selective laser melting, *International Journal of Thermal Sciences* 172 (2022) 107312.
- [24] R. P. Odele, V. Narayanan, E. Rasouli, Performance model of an additively manufactured micro-pin array solar thermal central receiver, *Solar Energy* 241 (2022) 621–636.
- [25] M.-S. Kim, K.-S. Lee, The thermoflow characteristics of an oscillatory flow in offset-strip fins, *Numerical Heat Transfer, Part A: Applications* 58 (11) (2010) 835–851.
- [26] S. Patankar, C. Liu, E. Sparrow, Fully developed flow and heat transfer in ducts having streamwise-periodic variations of cross-sectional area, *Journal of Heat Transfer—Transactions of the ASME* 99 (1977) 180–186.
- [27] S. Whitaker, The forchheimer equation: a theoretical development, *Transport in Porous media* 25 (1) (1996) 27–61.

- [28] M. Quintard, M. Kaviany, S. Whitaker, Two-medium treatment of heat transfer in porous media: numerical results for effective properties, *Advances in water resources* 20 (2-3) (1997) 77–94.
- [29] A. Nakayama, F. Kuwahara, T. Hayashi, Numerical modelling for three-dimensional heat and fluid flow through a bank of cylinders in yaw, *Journal of Fluid Mechanics* 498 (2004) 139–159.
- [30] C. T. DeGroot, A. G. Straatman, Closure of non-equilibrium volume-averaged energy equations in high-conductivity porous media, *International journal of heat and mass transfer* 54 (23-24) (2011) 5039–5048.
- [31] G. Buckinx, M. Baelmans, Multi-scale modelling of flow in periodic solid structures through spatial averaging, *Journal of Computational Physics* 291 (2015) 34–51.
- [32] G. Buckinx, M. Baelmans, Macro-scale heat transfer in periodically developed flow through isothermal solids, *Journal of Fluid Mechanics* 780 (2015) 274–298.
- [33] G. Buckinx, M. Baelmans, Macro-scale conjugate heat transfer in periodically developed flow through solid structures, *Journal of Fluid Mechanics* 804 (2016) 298–322.
- [34] G. Buckinx, Macro-scale flow and heat transfer in systems with periodic solid structures, Ph.D. thesis, KU Leuven (1 2017).
- [35] M. Quintard, S. Whitaker, Transport in ordered and disordered porous media i: The cellular average and the use of weighting functions, *Transport in porous media* 14 (2) (1994) 163–177.
- [36] M. Quintard, S. Whitaker, Transport in ordered and disordered porous media ii: Generalized volume averaging, *Transport in porous media* 14 (2) (1994) 179–206.
- [37] M. Quintard, S. Whitaker, Transport in ordered and disordered porous media iii: Closure and comparison between theory and experiment, *Transport in Porous Media* 15 (1) (1994) 31–49.

- [38] M. Quintard, S. Whitaker, Transport in ordered and disordered porous media iv: Computer generated porous media for three-dimensional systems, *Transport in porous media* 15 (1) (1994) 51–70.
- [39] Y. Davit, M. Quintard, Technical notes on volume averaging in porous media i: how to choose a spatial averaging operator for periodic and quasiperiodic structures, *Transport in Porous Media* 119 (3) (2017) 555–584.
- [40] A. Vangeffelen, Macro-scale modeling of compact heat transfer devices with offset strip fins, Ph.D. thesis, KU Leuven (6 2023).
- [41] F. Feppon, Asymptotic expansions of Stokes flows in finite periodic channels, working paper or preprint (2024).
URL <https://hal.archives-ouvertes.fr/hal-04443652>
- [42] v. L. Graetz, Ueber die wärmeleitungsfähigkeit von flüssigkeiten, *Annalen der Physik* 254 (1) (1882) 79–94.
- [43] v. L. Graetz, Über die wärmeleitungsfähigkeit von flüssigkeiten, *Annalen der Physik* 261 (7) (1885) 337–357.
- [44] W. Nusselt, Die abhängigkeit der wärmeübergangszahl von der rohrlänge, *VDI*, 1910.
- [45] A. Lévêque, *Les lois de la transmission de chaleur par convection*, Dunod, 1928.
- [46] M. Awad, Heat transfer for laminar thermally developing flow in parallel-plates using the asymptotic method, in: *2010 3rd International Conference on Thermal Issues in Emerging Technologies Theory and Applications*, IEEE, 2010, pp. 371–387.
- [47] U. Grigull, H. Tratz, Thermischer einlauf in ausgebildeter laminarer rohrströmung, *International Journal of Heat and Mass Transfer* 8 (5) (1965) 669–678.
- [48] S. Montgomery, P. Wibulsvas, Laminar flow heat-transfer in ducts of rectangular cross-section, in: *International Heat Transfer Conference Digital Library*, Begel House Inc., 1966, pp. 104–112.

- [49] A. Tay, G. D. V. Davis, Application of the finite element method to convection heat transfer between parallel planes, *International Journal of Heat and Mass Transfer* 14 (8) (1971) 1057–1069.
- [50] C.-L. Hwang, L.-T. Fan, Finite difference analysis of forced-convection heat transfer in entrance region of a flat rectangular duct, *Applied Scientific Research, Section A* 13 (1) (1964) 401–422.
- [51] S. Montgomery, P. Wibulswas, Laminar flow heat transfer for simultaneously developing velocity and temperature profiles in ducts of rectangular cross section, *Applied Scientific Research* 18 (1) (1968) 247–259.
- [52] T. Nguyen, Incremental heat transfer number in the entry region of circular tubes, *International journal of heat and mass transfer* 36 (14) (1993) 3659–3662.
- [53] E. M. Sparrow, A. Garcia, W. Chuck, Numerical and experimental turbulent heat transfer results for a one-sided heated rectangular duct, *Numerical Heat Transfer, Part A: Applications* 9 (3) (1986) 301–322.
- [54] G. Buckinx, A. Vangheffelen, Quasi-periodically developed flow in channels with arrays of in-line square cylinders (2023). [arXiv:2306.14201](https://arxiv.org/abs/2306.14201).
- [55] G. Buckinx, A macro-scale description of quasi-periodically-developed flow (2022). [arXiv:2202.08245](https://arxiv.org/abs/2202.08245).
- [56] G. Buckinx, A mathematical description of the quasi-periodically developed heat transfer regime in channels with arrays of periodic solid structures (2024). [arXiv:2403.16960](https://arxiv.org/abs/2403.16960).
- [57] J. Dong, J. Chen, Z. Chen, Y. Zhou, Air-side thermal hydraulic performance of offset strip fin aluminum heat exchangers, *Applied Thermal Engineering* 27 (2-3) (2007) 306–313.
- [58] A. Vangheffelen, G. Buckinx, C. M. De Servi, M. R. Vetrano, M. Baelmans, Developed and quasi-developed macro-scale flow in micro- and mini-channels

- with arrays of offset strip fins, *Physics of Fluids* 35 (7) (2023) 073611.
doi:10.1063/5.0156697.
- [59] R. K. Shah, D. P. Sekulic, *Fundamentals of heat exchanger design*, John Wiley & Sons, 2003.
- [60] E. W. Weisstein, Rectangle function, <https://mathworld.wolfram.com/>.
- [61] M. S. Alnæs, J. Blechta, J. Hake, A. Johansson, B. Kehlet, A. Logg, C. Richardson, J. Ring, M. E. Rognes, G. N. Wells, The fenics project version 1.5, *Archive of Numerical Software* 3 (100). doi:10.11588/ans.2015.100.20553.
- [62] S. Balay, S. Abhyankar, M. F. Adams, S. Benson, J. Brown, P. Brune, K. Buschelman, E. M. Constantinescu, L. Dalcin, A. Dener, V. Eijkhout, J. Faibussowitsch, W. D. Gropp, V. Hapla, T. Isaac, P. Jolivet, D. Karpeev, D. Kaushik, M. G. Knepley, F. Kong, S. Kruger, D. A. May, L. C. McInnes, R. T. Mills, L. Mitchell, T. Munson, J. E. Roman, K. Rupp, P. Sanan, J. Sarich, B. F. Smith, S. Zampini, H. Zhang, H. Zhang, J. Zhang, PETSc Web page, <https://petsc.org/> (2023).
URL <https://petsc.org/>
- [63] J. Ahrens, B. Geveci, C. Law, ParaView: An end-user tool for large data visualization, in: *Visualization Handbook*, Elsevier, 2005, ISBN 978-0123875822.
- [64] D. L. Penha, S. Stolz, J. G. Kuerten, M. Nordlund, A. K. Kuczaj, B. J. Geurts, Fully-developed conjugate heat transfer in porous media with uniform heating, *International journal of heat and fluid flow* 38 (2012) 94–106.
- [65] M. Everts, J. P. Meyer, Laminar hydrodynamic and thermal entrance lengths for simultaneously hydrodynamically and thermally developing forced and mixed convective flows in horizontal tubes, *Experimental Thermal and Fluid Science* 118 (2020) 110153.
- [66] Y. S. Muzychka, M. M. Yovanovich, Laminar flow friction and heat transfer in non-circular ducts and channels part ii: Thermal problem, *Compact Heat Exchangers: A Festschrift on the 60th Birthday of Ramesh K. Shah* (2002).

- [67] P.-S. Lee, S. V. Garimella, Thermally developing flow and heat transfer in rectangular microchannels of different aspect ratios, *International journal of heat and mass transfer* 49 (17-18) (2006) 3060–3067.
- [68] H. Ma, Z. Duan, X. Ning, L. Su, Numerical investigation on heat transfer behavior of thermally developing flow inside rectangular microchannels, *Case Studies in Thermal Engineering* 24 (2021) 100856.
- [69] H. Schlichting, J. Kestin, *Boundary layer theory*, Vol. 121, Springer, 1961.
- [70] A. Hachemi, Experimental study of thermal performance of offset rectangular plate fin absorber-plates, *Renewable Energy* 17 (3) (1999) 371–384.